ACS Infectious Diseases

pubs.acs.org/journal/aidcbc
Article

Identification of Innovative Folate Inhibitors Leveraging the Amino Dihydrotriazine Motif from Cycloguanil for Their Potential as Anti-*Trypanosoma brucei* Agents

Published as part of ACS Infectious Diseases virtual special issue "One Health and Vector Borne Parasitic Diseases".

Valeria Francesconi, Marco Rizzo, Cecilia Pozzi, Lorenzo Tagliazucchi, Claude U. Konchie Simo, Giulia Saporito, Giacomo Landi, Stefano Mangani, Anna Carbone, Silvia Schenone, Nuno Santarém, Joana Tavares, Anabela Cordeiro-da-Silva, Maria Paola Costi, and Michele Tonelli*

Cite This: *ACS Infect. Dis.* 2024, 10, 2755−2774

ABSTRACT: Folate enzymes, namely, dihydrofolate reductase (DHFR) and pteridine reductase (PTR1) are acknowledged targets for the development of antiparasitic agents against Trypanosomiasis and Leishmaniasis. Based on the amino dihydrotriazine motif of the drug Cycloguanil (Cyc), a known inhibitor of both folate enzymes, we have identified two novel series of inhibitors, the 2-amino triazino benzimidazoles (**1**) and 2-guanidino benzimidazoles (**2**), as their open ring analogues. Enzymatic screening was carried out against PTR1, DHFR, and thymidylate synthase (TS). The crystal structures of *Tb*DHFR and *Tb*PTR1 in complex with selected compounds experienced in both cases a substrate-like binding mode and allowed the rationalization of the main chemical features supporting the inhibitor ability to target folate enzymes. Biological evaluation of both series was performed against *T. brucei* and *L. infantum* and the toxicity against THP-1 human macrophages. Notably, the 5,6-dimethyl-2-guanidinobenzimidazole **2g** resulted to be the most potent (K_i = 9 nM) and highly selective *Tb*DHFR inhibitor, 6000-fold over *Tb*PTR1 and 394-fold over *h*DHFR. The 5,6-dimethyl tricyclic analogue **1g**, despite showing a lower potency and selectivity profile than **2g**, shared a comparable antiparasitic activity against *T. brucei* in the low micromolar domain. The dichloro-substituted 2-guanidino benzimidazoles **2c** and **2d** revealed their potent and broad-spectrum antitrypanosomatid activity affecting the growth of *T. brucei* and *L. infantum* parasites. Therefore, both chemotypes could represent promising templates that could be valorized for further drug development.

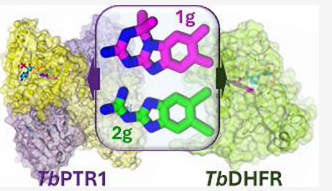

KEYWORDS: *antiparasitic agents, dihydrofolate reductase inhibitors, pteridine reductase inhibitors, triazino and guanidino benzimidazoles, Trypanosoma brucei, Leishmania infantum*

Human African trypanosomiasis (HAT, also known as sleeping sickness) belongs to the group of neglected tropical diseases (NTDs) which affect about one billion people worldwide[1] and cause significant morbidity and mortality in humans and animals.[2] Two subspecies of parasite cause different disease courses in humans: *Trypanosoma brucei* gambiense is responsible for the chronic and slow-progressing form of the disease, while *Trypanosoma brucei* rhodesiense establishes an acute, faster-progressing, and multiorgan illness.[3] To date, control programs have considerably reduced the occurrence of HAT, although it still represents a public health concern until its complete elimination is reached. World Health Organization (WHO) has set this achievement for 2030,[4,5] asking for cooperation among multiple sectors, on the basis of the One Health approach.

Only six drugs are in clinics for HAT, whose indications for use depend on the stage of the infection, i.e., melarsoprol, suramin, pentamidine, eflornithine, nifurtimox/eflornithine, and the most recent fexinidazole.[6,7] However, the lack of effective treatment due to the toxicity and resistance phenomena are the main hurdles and have prompted researchers to seek more efficacious, safe, and unexpensive drugs.[8,9] Along with *T. brucei*, the *Trypanosomatidae* family includes *T. cruzi* and *Leishmania* parasites which are the etiologic agents of Chagas disease and leishmaniasis, respectively. The diseases caused by these protozoa are a major public health problem in many parts of the world and call for the need of renovating the arsenal of medications, being still restricted to quite obsolete solutions.[10,11]

Received: February 9, 2024
Revised: May 6, 2024
Accepted: June 11, 2024
Published: July 2, 2024

https://doi.org/10.1021/acsinfecdis.4c00113
ACS Infect. Dis. 2024, 10, 2755−2774

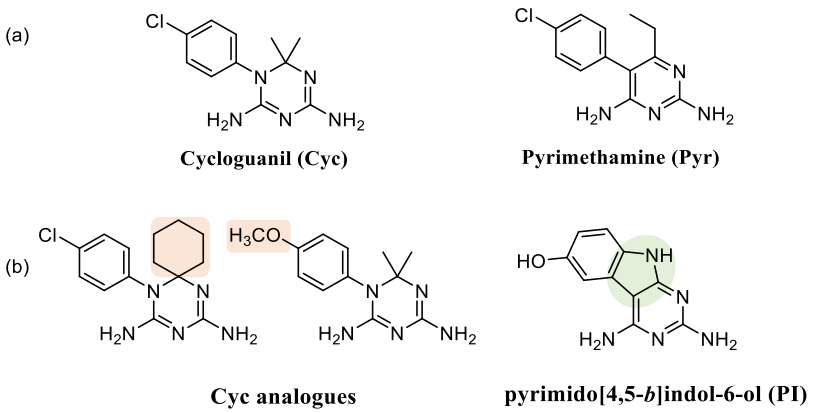

Figure 1. (a) Antiprotozoal drugs Cyc and Pyr, as template molecules targeting *Tb*DHFR and *Tb*PTR1; (b) previously studied *Tb*PTR1 inhibitors characterized by a key substitution on the core structure of Cyc or by a pyrimidine-based tricyclic scaffold (PI).

In recent years, targeting the enzymes of folate metabolism was demonstrated to be a successful strategy also for the treatment of parasitic infections such as Malaria, Leishmaniasis, and Trypanosomiasis.[12−14] Two enzymes, namely, dihydrofolate reductase (DHFR) and pteridine reductase 1 (PTR1), can provision the parasite of reduced folate (tetrahydrofolate, THF), a crucial cofactor in the synthesis of de novo nucleobases and certain amino acids to sustain its proliferation. DHFR is the primary enzyme in the folate path, while PTR1 participates for about 10%; when DHFR is inhibited, e.g., by the antifolate drug methotrexate (MTX), the amplification of both DHFR and PTR1 genes occurs to supply the parasite of folate metabolites.[15,16] Further investigations are in due course to incorporate more in-depth knowledge about the fine interplay between the two enzymes and the respective pathway connection. In contrast to humans, trypanosomatids express the DHFR as a homodimer comprising thymidylate synthase (bifunctional DHFR-TS), which catalyzes the reductive methylation of deoxyuridine monophosphate (dUMP) to thymidylate (dTMP) for DNA synthesis and repair. Notably, a recent study reinforced the druggability of *Tb*TS and, concurrently, the development of *Tb*TS inhibitors, from the observation that the anticancer drug nolatrexed, a known inhibitor of human TS (*h*TS, K_i = 15 nM), similarly inhibited *Tb*TS (K_i = 39.4 nM) and the growth of parasites (EC_{50} ∼ 32 μM, as the mean value from four diverse culture media).[17]

Folate-dependent enzymes have gained a lot of attention as the valued targets for addressing new treatments for HAT[9,14,18,19] and, despite numerous efforts, a moderate antiparasitic effect was observed for the distinct chemotypes developed so far, while demonstrating nanomolar potency against one of these two enzymes. Therefore, these findings support the concept that both PTR1 and DHFR should be targeted simultaneously and, possibly, to an equal extent.[13,15,20]

Monocyclic and bicyclic aromatic systems such as pyrimidines, pteridines, quinolines, pyrrolo-pyrimidines, benzimidazoles, and benzothiazoles, mimicking the substrate pterin moiety, were extensively studied as molecular scaffolds for the design of *Tb*PTR1 and *Tb*DHFR inhibitors.[13,21−24] Also, the antimalarial drug cycloguanil (Cyc) (Figure 1a), featured by a dihydrotriazine core, was found to target *Tb*PTR1 besides *Plasmodial and Trypanosoma* DHFR.[25] Interestingly, Cyc exhibited a superior affinity for *Tb*DHFR (K_i = 256 nM[26]) than *Tb*PTR1 (IC_{50} = 31.6 μM[25]) and a low antiparasitic effect against *T. brucei* (EC_{50} > 25 μM[26]). Conversely, some structurally related analogues of Cyc (Figure 1b), where the 4-Cl atom on the phenyl ring and/or the *gem*-dimethyl groups at C(6) were modified, showed an opposite trend of selectivity more favorable for *Tb*PTR1 than *Tb*DHFR.[27] In particular, a 4-OCH_3 on the phenyl ring (*Tb*DHFR IC_{50} = 33.2 μM, *Tb*PTR1 IC_{50} = 0.67 μM) and a bulky spiro-cyclohexyl moiety on C(6) (*Tb*DHFR IC_{50} = 17.6 μM, *Tb*PTR1 IC_{50} = 1.22 μM) improved the inhibitory performance against *Tb*PTR1 with respect to the prototype Cyc. These data suggested that the enzyme catalytic cavity could also accommodate more expanded molecular cores. The 2,4-diamino pyrimido[4,5-*b*]indole derivative (PI) (Figure 1b) was described as the first tricyclic compound targeting *Tb*PTR1 (K_i of 83 μM). In the complex with the enzyme, it unveiled an interaction network similar to pyrimethamine (Pyr) (Figure 1a) and Cyc, but it formed additional contacts within the hydrophobic pockets placed nearby in the catalytic site of *Tb*PTR1.[21]

Following the above consideration, in the present paper, we describe the design and synthesis of a new library of 2-aminotriazino[1,2-*a*]benzimidazoles and 2-guanidinobenzimidazoles. The biological profiling of the conceived set first included the evaluation of their on-target activities (*Tb*PTR1 and *Tb*DHFR). Then, we reasoned to examine the activity against *Tb*TS, considering the potential risk of toxic effects as a consequence of a 60% sequence identity to its human ortholog and an active site showing an identical amino acid sequence.[18] To estimate the toxicity and species-specificity preferences of the library, the human DHFR (*h*DHFR) and *h*TS inhibitions were then assessed. Most of the title compounds were assayed for their ability to inhibit *T. cruzi* and *L. major* DHFR enzymes with the aim of developing broad-spectrum antiprotozoan agents. The structures of *Tb*PTR1 and *Tb*DHFR were solved in complex with selected inhibitors and compared with those of Pyr and Cyc to explain the structure−activity relationships of these new compound series. Finally, the antiparasitic effect (EC_{50}) of both series was evaluated against *T. brucei* brucei and *L. infantum* promastigotes and the toxicity (CC_{50}) against THP-1 human macrophages as a representative model of the host defense immune response against parasite infection.

RESULT AND DISCUSSION

Design of the Compounds. Evidence from the literature provides several cocrystal structures of *Tb*PTR1 with distinct molecules, while only few examples of *Tb*DHFR−inhibitor complexes are resolved. While for the known drug Pyr the

https://doi.org/10.1021/acsinfecdis.4c00113
ACS Infect. Dis. 2024, 10, 2755−2774

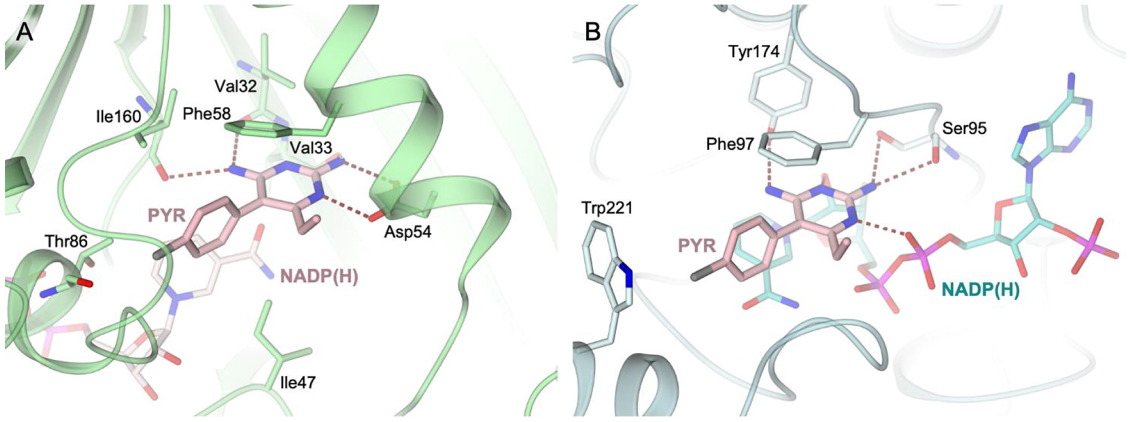

Figure 2. Active site view of the complexes (A) *Tb*DHFR-NADP(H) (light green cartoon and carbons; cofactor in sticks, light pink carbons) and Pyr (in sticks, pink carbons), PDB id 3QFX;[26] (B) *Tb*PTR1-NADP(H) (light cyan cartoon and carbons; cofactor in sticks, cyan carbons) and Pyr (in sticks, pink carbons), PDB id 7OPJ.[27] In both panels, oxygen atoms are colored red, nitrogen blue, sulfur yellow, and phosphorus magenta. H-bonds are shown as tan dashed lines.

Table 1. Chemical Structures of the Compound's Library (1a−g and 2a−g) Investigated as Antiprotozoal Agents

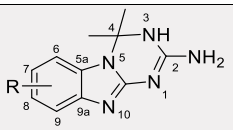

Triazino benzimidazoles

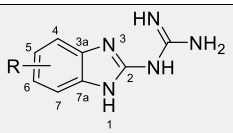

2-Guanidino benzimidazoles

triazino benzimidazoles		2-guanidino benzimidazoles	
comp.	R	comp.	R
1a	H	**2a**	H
1b	7(8)-Cl	**2b**	5(6)-Cl
1c	7,8-diCl	**2c**	5,6-diCl
1d	7,9-diCl	**2d**	4,6-diCl
1e	7(8)-CF_3	**2e**	5(6)-CF_3
1f	7(8)-OCH_3	**2f**	5(6)-OCH_3
1g	7,8-diCH_3	**2g**	5,6-diCH_3

complexes with both enzymes are released, for Cyc only that with *Tb*PTR1 is available. The two antifolate drugs differ in the chemical structure of the core, i.e., the pyrimidine ring of Pyr and the nonaromatic 1,6-dihydrotriazine ring of Cyc. They adopt similar binding modes within the *Tb*PTR1 active site, entailing the same network of H-bonds and hydrophobic interactions,[27] as discussed below. Therefore, the structures of DHFR and PTR1 complexes with Pyr were chosen as template models for the design of the novel compound's library, and the derived information was used for the purpose of a meaningful comparison.

Despite DHFR and PTR1 performing analogous catalytic reactions, recognizing the same substrates, their active sites are structurally distinct and exhibit only a little consensus. Moreover, the comparison between the structures of their complexes with Pyr has allowed the identification of the main structural determinants responsible for common interactions toward both enzymes.

In *Tb*DHFR, the binding of Pyr is stabilized through a network of H-bonds entailed with Val32 (backbone carbonyl group) and Ile160 (backbone carbonyl group), on one side, and with Asp54, on the other (Figure 2A). The inhibitor is further stabilized by van der Waals contacts with Ile47, Phe58, and Ile160 and by a halogen bond with Thr86. In *Tb*PTR1, Pyr binds inside the peculiar π-sandwich lined by the cofactor nicotinamide and the aromatic side chain of Phe97 (Figure 2B). Inside the catalytic cavity, the inhibitor is further stabilized by the H-bonds entailed with Ser95 (hydroxyl and backbone carbonyl groups), Tyr174 (hydroxyl group), and the cofactor (ribose hydroxyl and β-phosphate groups) and by the halogen bond with Trp221 (indole moiety).

On the wave of these findings, we considered it interesting to synthesize a novel set of compounds (Table 1), the 2-aminotriazino[1,2-*a*]benzimidazoles (**1a−g**), that were obtained through the scaffold hopping manipulation of Cyc, leading to a new tricyclic system where the key amino dihydrotriazine motif of Cyc was integrated with the benzimidazole ring. Noteworthy, benzimidazole is regarded as a "privileged structure" in heterocyclic chemistry due to its association with a wide range of biological activities.[28,29] In the field of antiprotozoan agents, it recurs in several examples as the primary unit or meaningful substructure.[30−32]

Further, their open ring analogues, the 2-guanidino benzimidazoles **2a−g**, were included in the study, as pseudoring structures that may exhibit some conformational analogy with 2-aminotriazino benzimidazoles owing to a greater flexibility.

https://doi.org/10.1021/acsinfecdis.4c00113
ACS Infect. Dis. 2024, 10, 2755−2774

The novel chemotypes were decorated with a Cl atom, as in PYR (Figure 2) and CYC, with a view to preserving the ability of the prototypes to entail a halogen bond with the respective amino acid residues (Thr86 and Trp221) of the *Tb*DHFR and *Tb*PTR1 active sites. Besides exploring the lipophilic CF_3 and CH_3 groups on the aromatic ring, which are reciprocally characterized by an opposite inductive electronic effect, the polar and electron-donor OCH_3 group was also considered (Table 1), since it previously demonstrated to improve the inhibition of *Tb*PTR1 when replacing the 4-Cl atom of Cyc[27] (Figure 1).

Chemistry. The 2-guanidino benzimidazoles **2a−g** were synthesized by reacting the proper 1,2-phenylendiamine with dicyandiamide in acid-catalyzed conditions (Scheme 1), while

Scheme 1. Reagents and Conditions: (i) HCl Conc. (1 Eq), H_2O, Reflux 6 h

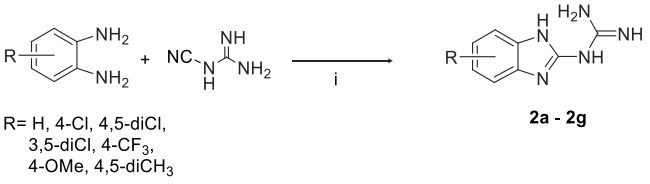

their respective 2-aminotriazino[1,2-*a*]benzimidazole derivatives of series **1** were achieved through a ring annellation reaction of series **2** with acetone under piperidine catalysis (Scheme 2).

The triazino benzimidazole **1a** and 2-guanidino benzimidazoles **2a−c**, **2e**, and **2f** were previously obtained.[33,34] Compounds **2a-c**, **2e**, and **2f**[33] were reported as free base and/or salts and were characterized only by melting point and elemental analysis related to C and H. Herein, we report the structural elucidation in more detail, including ^{1}H and ^{13}C NMR.

Based on NMR spectra, cycloaddition of acetone to compounds **2** (**2b**, **2e**, and **2f**) did not show regioselectivity and gave the corresponding tricyclic compounds **1** as a 60/40 mixture of isomers **I** and **II**, respectively, namely, **1b-I** and **1b-II**, **1e-I**, and **1e-II** and **1f-I** and **1f-II** (Scheme 2).

The assignment of each specific isomeric peak and the definition of the proportions between the two isomers in the ^{1}H NMR spectra, COSY, and NOESY experiments were consistent with the previous findings of Dolzhenko et al. relative to a structural analogue of series 1, namely, the 7(8)-methyl triazino[1,2-*a*]benzimidazole.[34] The electronic nature of the R substituent in series **2** did not significantly influence the ring closure taking place at N-1 of benzimidazole and N-3 of the guanidino moiety; in fact, the isomer **II**, carrying the substituent at C(7) of the tricyclic scaffold always formed in a lower percentage than isomer **I**, that is substituted at C(8). The 3:2 ratio between the two isomers may be due to the steric hindrance exerted by the *gem*-dimethyl group of acetone during the formation of the dihydrotriazine ring, from which the R substituent of the guanidino benzimidazole preferentially arranges farther away.

In the ^{1}H NMR spectrum, the C(6)−H signals of triazino[1,2-*a*]benzimidazole derivatives always display the highest chemical shift values among all the aromatic hydrogens as a result of the deshielding effect caused by their proximity to the *gem*-diCH_3 groups.

The NMR spectra of the asymmetric disubstituted compound **1d** allowed observation of the yield of only one reaction product. Dolzhenko and Chui previously described the formation of a cross-peak in the NOESY-2D spectra for the aromatic C(6)−H signal and the H atoms of the two *gem*-diCH_3 groups at C(4).[34] In our NOESY-2D and 1D experiments, a strong cross-peak for the doublet at 7.41 at C(6) and the singlet at 1.74 (*gem*-diCH_3) appeared, confirming the exclusive formation of the 7,9-diCl isomer as **1d**.

Since the attempt to separate the two isomers of **1f**, such as representative samples of series **1**, by HPLC (gradient elution with a binary solution—eluent A: H_2O/HCOOH 0.1% v/v, eluent B: ACN/HCOOH 0.05% v/v) gave a negative result (see the HPLC chromatogram in SI), the 7(8)-monosubstituted triazino benzimidazoles **1b**, **1e**, and **1f** were tested as a congeners' mixture in biological and crystallographic experiments.

Regarding the ^{13}C NMR spectra of 2-gauanidino benzimidazoles **2**, the signals of carbons 3a, 7a, 4, and 7 are subject to extensive broadening and difficult to be attributed, as already depicted for **2a**.[35] This could be due to the prototropic interconversion among the 3 tautomeric forms and 14 isomers in which the 2-guanidino benzimidazole nucleus may exist;[36] an analogous phenomenon was previously highlighted also for the 3 tautomeric forms of the triazino[1,2-*a*]benzimidazole scaffold.[34]

Structure−Activity Relationship Studies against Parasitic and Human Enzymes. The triazino benzimidazoles (**1**) and 2-guanidino benzimidazoles (**2**) were tested in enzymatic inhibition assays to investigate their activity profiles against *Tb*PTR1 and *Tb*DHFR (Table 2) seeking dual targeting anti-*T. brucei* agents. For comparison, the compounds' activities toward *Lm*DHFR and *Tc*DHFR were also

Scheme 2. Reagents and Conditions: (i) 0.5 Eq of Piperidine, Reflux 7 h

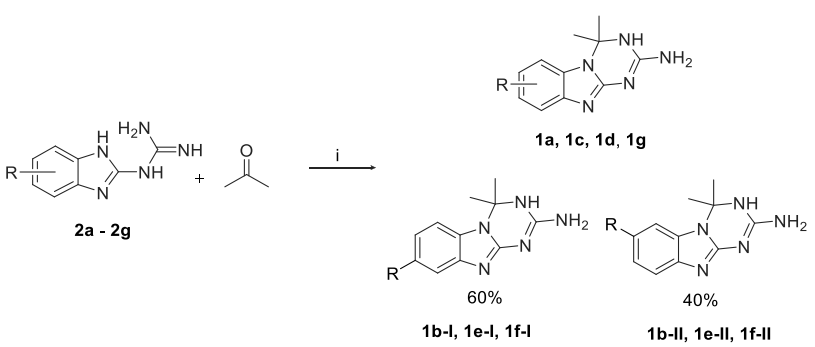

https://doi.org/10.1021/acsinfecdis.4c00113
ACS Infect. Dis. 2024, 10, 2755−2774

Table 2. Inhibition Constant (K_i) of Series (1) and (2) against *Tb*PTR1 and DHFR Enzymes[a]

	enzymatic screening									
cmp	*Tb*PTR1 K_i (μM)	*Tb*DHFR K_i (μM)	*Tb*TS K_i (μM)	*h*DHFR K_i (μM)	*h*TS K_i (μM)	selectivity K_i *Tb*PTR1/K_i *Tb*DHFR	species selectivity K_i *h*DHFR/K_i *Tb*DHFR	species selectivity K_i *h*TS/K_i *Tb*TS	*Lm*DHFR K_i (μM)	*Tc*DHFR K_i (μM)
1a	12.7	0.070	30.0	3.78	>500	181	54	>17	0.48	9.66
1b	27.0	0.459	46.5	1.52	>500	59	3.3	>11	0.54	0.94
1c	50.6	0.339	9.77	0.663	>500	149	2.0	>51	1.20	1.07
1d	34.2	0.336	44.3	1.35	>500	102	4.0	>11	0.16	2.29
1e	36.4	0.758	58.6	11.2	>500	48	15	>8.5	26	7.41
1f	5.73	0.065	33.7	11.9	>500	88	183	>15	14.3	11.0
1g	7.89	1.09	22.0	1.05	>500	7.2	0.96	>23	2.45	1.38
2a	13.3	0.029	23.6	2.21	>500	459	76	>21	-	-
2b	21.1	0.070	36.0	2.77	>500	301	40	>14	0.58	10.6
2c	3.23	0.66	50.3	1.51	>500	4.9	2.3	>9.9	1.58	-
2d	4.94	0.113	20.3	4.36	>500	44	39	>25	-	-
2e	17.8	0.038	21.0	2.12	>500	468	56	>24	-	-
2f	9.15	0.131	44.6	18.1	>500	70	138	>11	-	-
2g	54.0	0.009	18.2	3.55	>500	6000	394	>27	1.04	0.60
Cyc	4.16	0.256	-	0.396	22.5	16	1.55	-	-	-
Pyr	0.016	0.038	-	0.247	11.8	0.4	6.50	-	-	-
MTX	0.138	0.006	46.3[b]	0.004	1.57	23	0.67	0.03	-	-

[a]Selectivity index for compounds **1** and **2** for K_i obtained against *Tb*PTR1 vs *Tb*DHFR, *h*DHFR vs *Tb*DHFR, and *h*TS vs *Tb*TS. Activity is compared with that of Cyc, Pyr, and MTX, as reference drugs. All the compounds demonstrated <10% inhibition activity when tested up to 200 μM against *h*TS. [b]K_i value from Gibson et al.[17].

Table 3. Antiparasitic Activities (EC_{50}), Cytotoxicity (CC_{50}), and Selectivity Index (SI)[a,b]

	cell-based biological screening					
cmp	*T. brucei* EC_{50} (μM)	*T. brucei* EC_{50} (μM) folate deficiency	THP-1 CC_{50} (μM)	SI CC_{50}/EC_{50}	SI CC_{50}/EC_{50} folate deficiency	*L. infantum* EC_{50} (μM)
1a	>20	>20	>100	//	//	>20
1b	>20	>20	>100	//	//	>20
1c	>20	>20	>50	//	//	>20
1d	>20	>20	>100	//	//	>20
1e	>20	>20	>100	//	//	>20
1f	>20	>20	>100	//	//	>20
1g	6.63	18.2	>100	15.1	5.50	>20
2a	>20	>20	>100	//	//	>20
2b	15.2	15.2	>100	6.58	6.60	>20
2c	7.8	6.52	95.3	12.2	14.6	22.5
2d	2.91	5.97	>100	34.4	16.8	6.62
2e	18.2	>20	>100	5.50	//	>20
2f	>20	>20	>100	//	//	>20
2g	14.5	13.8	>100	6.91	7.2	>20
CYC	>80	27.2	221	//	8.12	>80
PYR	17.3	2.08	105	6.07	50.4	99.2
MTX	23.3	0.0054	-	//	//	-
PENT	0.0041	-	-	//	//	-
MLF	-	-	-	//	//	10.9

[a]Data are from three independent experiments and are expressed as mean; SD < 10%. [b]- represents not determined; // represents not detectable at the maximum compound solubility.

evaluated. The kinetic inhibition experiments were conducted by determining the IC_{50} for each compound in appropriate experimental conditions suitable for deriving the corresponding K_i, assuming a competitive inhibition pattern, as reported in the Methods section. The competitive inhibition was supported by the X-ray crystal structures of the obtained protein/inhibitor complex in which the inhibitor was replacing the enzyme substrate. In the case of PTR1, the replaced substrate was DHB, while in DHFRs, the replaced substrate was DHF. Deepening the mechanistic aspects of the enzyme inhibition for all compounds was out of the scope of this work.

In general, the 2-guanidino benzimidazoles **2** resulted to be more potent than tricyclic derivatives **1**, being able to steer their structural flexibility and the related binding ability to *T. brucei* enzymes. For both series, a preferential inhibition profile *versus* *Tb*DHFR over *Tb*PTR1 was observed, as demonstrated by the submicromolar/nanomolar potencies reached against *Tb*DHFR that worsened from at least one up to 3 orders of magnitude against *Tb*PTR1. Regarding the impact on the

https://doi.org/10.1021/acsinfecdis.4c00113
ACS Infect. Dis. 2024, 10, 2755−2774

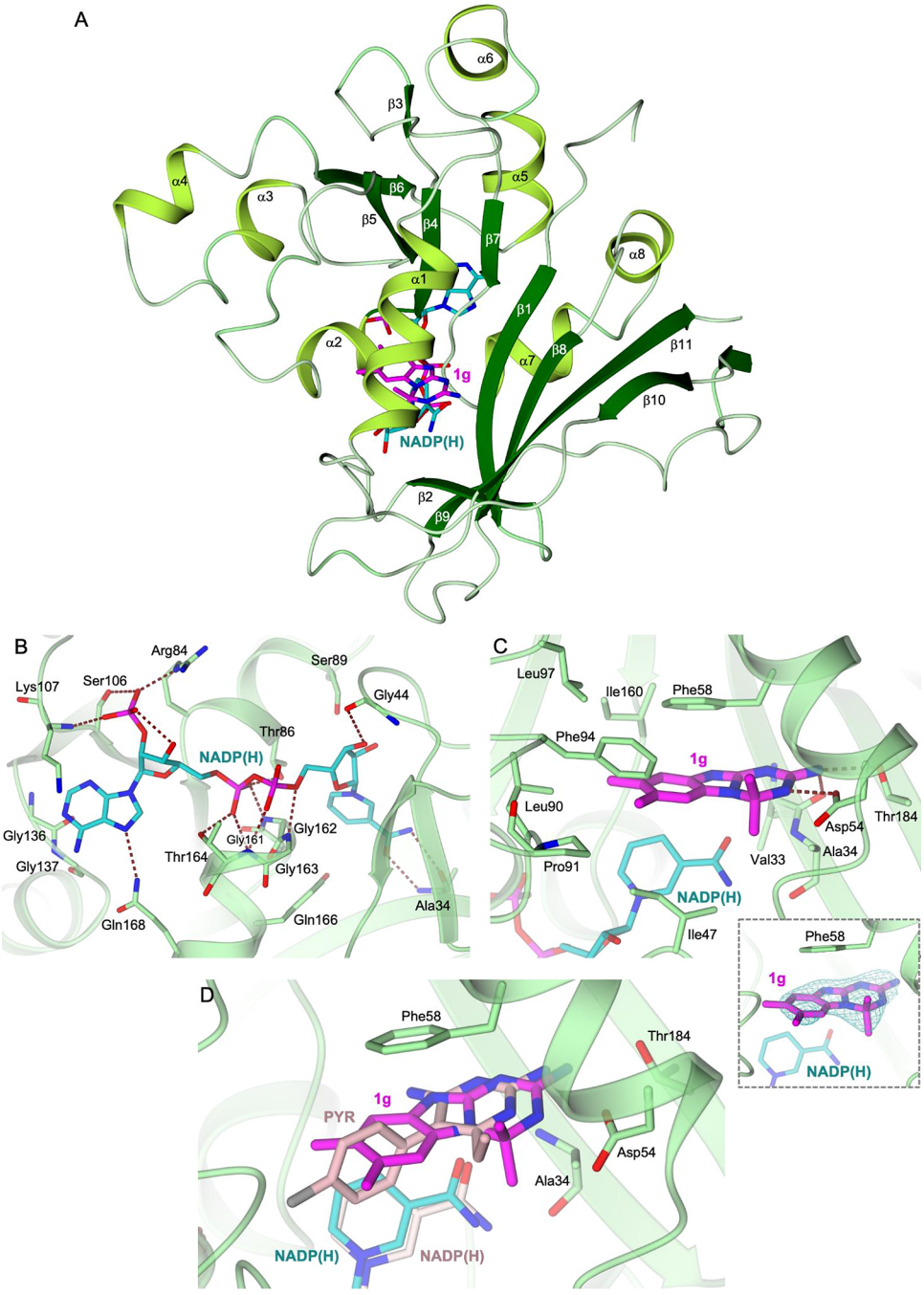

Figure 3. Crystal structure of *Tb*DHFR (light green cartoon and carbons) in the ternary complex with the cofactor NADP(H) (in sticks, turquoise carbons) and **1g** (in sticks, magenta carbons). (A) Overall fold of *Tb*DHFR (α-helices and β-strands are colored yellow-green and dark green, respectively). (B) View of the cofactor biding site. (C) Active site view, showing binding of **1g**; the inhibitor surrounded by the omit map (green mesh contoured at the 2.5σ level) is displayed in the inset. (D) Active site view of the superimposition between the complexes *Tb*DHFR-NADP(H)-**1g** and *Tb*DHFR-NADP(H)-Pyr (cofactor and Pyr in sticks, pink carbons; PDB id 3QFX).[26] In all panels, oxygen atoms are colored red, nitrogen blue, sulfur yellow, and phosphorus magenta. H-bonds are shown as tan dashed lines.

activity exerted by the chemical nature (polar or apolar) and electronic effect (electron-withdrawing or -donating) of the substituents considered, it can be observed that there is no correlation between the two series; indeed, a more prominent contribution to the inhibition activity against *Tb*DHFR seems to be ruled by the steric effect of the substituent in combination with the bicyclic or tricyclic structure of the scaffold. Within the triazino benzimidazoles, the unsubstituted derivative **1a** (K_i = 70 nM) and the 7(8)-OCH_3 derivative **1f** (K_i = 65 nM) were the most potent molecules, while among the open ring guanidino benzimidazoles the unsubstituted derivative **2a** (K_i = 29 nM) and 5(6)-CF_3 **2e** (K_i = 38 nM), all matching the nanomolar potency of Pyr toward *Tb*DHFR (K_i = 38 nM). In addition, even better was the 5,6-dimethyl-2-guanidino benzimidazole **2g** exhibiting a K_i of 9 nM against *Tb*DHFR, which compared the potency of MTX (K_i = 6 nM). With respect to MTX, showing a selectivity index of 23 as the ratio between the K_i values of *Tb*PTR1 and *Tb*DHFR, compound **2g** elicited interest for its very unbalanced inhibition profile, 6000-fold more favorable for *Tb*DHFR

https://doi.org/10.1021/acsinfecdis.4c00113
ACS Infect. Dis. 2024, 10, 2755−2774

(Table 2). In perspective, this highly selective and potent *Tb*DHFR inhibitor is worthy of further investigations in drug combination tests with a potent and selective *Tb*PTR1 inhibitor, conceivably with a view to getting better management of HAT.

Besides the inhibition of DHFR, also that of TS can interfere with the DNA replication leading to cell death.[37] The activity of TS consists of the oxidation of N^5,N^{10}-methylene-tetrahydrofolate to DHF, and the methyl donor for the formation of dTMP from dUMP. These functions are unique to TS. Therefore, TS is notoriously recognized as a target for cancer therapy. Unlike mammals, protozoa cannot salvage thymidine and, thus, rely completely on the de novo thymidylate cycle by TS for the synthesis of dTMP.[38] However, since the human and parasite TS enzymes share a strong similarity at the primary-sequence level, it is argued that compounds active against the parasite would also be toxic to the host. Hence, the compounds were tested for the inhibition of the TS domain of the bifunctional *Tb*DHFR-TS. It is worth noting that all the K_i values for the compounds fall in the micromolar range as for the DHFR-targeting drugs Cyc, Pyr, and MTX (Table 2), markedly far from the nanomolar inhibition potency of the chemotherapy agent nolatrexed, which was designed to directly inhibit TS.[17] To ascertain the species selectivity of the present compounds, i.e., the preference for the protozoan *Tb*DHFR, the study of human DHFR (*h*DHFR) inhibition was also assessed. Both series showed micromolar inhibition constants against the *h*DHFR, except for the 7,8-dichloro triazino benzimidazole **1c**, which reached a value of 663 nM, which was comparable to those of Cyc and Pyr, but higher than that of MTX (K_i = 4 nM). Hence, a valuable safety profile for these molecules was pointed out, as confirmed by the absence of cytotoxicity (CC_{50} > 100 μM, Table 3) against THP-1 cells. Indeed, the submicromolar activity of **1c** against *h*DHFR matched up with the appearance of toxicity to the host (CC_{50} > 50 μM, Table 3). This observation was further corroborated by the calculation of the off-target activity on *h*TS. Indeed, all the compounds demonstrated <10% inhibition in kinetic assays when tested at 200 μM (Table 2).

By the analysis of the species-selectivity profile (Table 2), as the ratio K_i *h*DHFR/K_i *Tb*DHFR, MTX turned out to be almost equipotent toward both orthologues (SI = 0.67), in agreement with its clinical application as an anticancer, anti-inflammatory, and immunosuppressive agent. Analogous behavior was observed for Cyc (SI = 1.55), while Pyr manifested a ∼6.5-fold higher SI favoring the parasitic enzyme. The triazino benzimidazoles bearing a lipophilic substituent on the aromatic ring generally showed lower SI values ranging from 0.96 (**1g**) to 15 (**1e**), except for the unsubstituted derivative **1a** (SI = 54) and the even more promising 7(8)-OCH_3 analogue **1f** (SI = 183), both endowed with a marked preference for *Tb*DHFR. Apart from the 5,6-dichloro derivative **2c** (SI = 2.3), the 2-guanidino benzimidazoles (series **2**) performed better than Pyr, showing SI values up to the highest 394 for the 5,6-dimethyl derivative **2g**, that confirmed to be the most potent and selective *Tb*DHFR inhibitor. Intriguingly, as previously described for Cyc analogues depicted in Figure 1, the polar methoxy group confirmed its worthy impact on fostering the inhibition of the parasitic DHFR, thus allowing the yield of high values of selectivity for compounds **1f** and **2f**.

Concerning the other DHFRs from *L. major* and *T. cruzi*, the first enzyme seemed to be more sensitive as approximately 40% of the compounds tested showed submicromolar K_i values. The 7,9-diCl triazino benzimidazole (**1d**) and the unsubstituted analogue (**1a**) were found to be the most effective inhibitors of *Lm*DHFR with K_i values equal to 0.16 and 0.48 μM, respectively. Differently, the 5,6-dimethyl guanidino benzimidazole **2g**, the most active *Tb*DHFR inhibitor, was proven to be also the best inhibitor of *Tc*DHFR, but with a drop-off in potency of 67-fold (K_i = 0.60 μM). These encouraging data let envisage the validity of these chemotypes toward the development of broad-spectrum antiprotozoal agents.

The observed activity can be evaluated in a 3D structure obtained from the crystallization complexes of some of the best inhibitors with *Tb*DHFR and *Tb*PTR1 enzymes. In the next section, the structural analysis of the complexes is developed.

X-ray Crystallographic Structure of *Tb*DHFR. At first, the X-ray crystal structure of the *Tb*DHFR as apoenzyme was studied. Despite various attempts, we failed to crystallize the full-length *TbDHFR-TS* enzyme. On the other hand, we obtained crystals of the isolated *Tb*DHFR domain, covering the N-terminal region extending to residue 241. The structure of *Tb*DHFR was solved in complex with the cofactor NADP(H) and the inhibitor **1g** to 2.90 Å resolution, showing an enzyme monomer in the crystal asymmetric unit (Tables S1 and S2). The model was fully rebuilt apart for starting twenty-two N-terminal and the last two C-terminal residues. The *Tb*DHFR domain folds in 11 β-strands, eight α-helices, and one shorter 3_{10} helix (Figure 3A), showing a structure remarkably similar to formerly reported models.[26] The cofactor binds in an extended conformation, stabilized by a tight network of conserved interactions with the surrounding residues (Figure 3B). The adenine ring is enclosed in the pocket lined by Leu105 and Arg107 on the β4-α3 loop, Gly136 and Gly137 of loops β5-α5, and Gln168 on helix α7. The NADP(H) α-phosphate forms ionic bonds with Arg84 on helix α2 and is H-bonded to Ser106 of the β4-α3 loop, whereas the β and γ-phosphates entail H-bonds with Thr86 on helix α2 and the three starting residues of helix α7. The terminal ribose and nicotinamide moieties are accommodated in the pocket lined by Ala34 of strand β1, residues 41−47, belonging to strand β2 and the following loop β2-α1, Thr86, and Ser89 of helix α2, residues 160−161 of the β6-α7 loop, and Tyr166 on helix α7. Ala34 plays a key role in keeping the correct alignment of the cofactor nicotinamide inside the cavity; indeed, the NADP(H) amide moiety faces the peptide bonds of the residue, forming two H-bonds with it (Figure 3B).

Compound 1g Binding to the *Tb*DHFR Catalytic Cavity. We selected compound **1g** for crystallization purposes because it showed one of the most promising K_i values. The compound behaves as a competitive inhibitor of the enzyme with respect to the DHF substrate, and this is supported by the observed X-ray crystal structure of the complex *Tb*DHFR:**1g**. The inhibitor occupies the dihydrofolate pocket, located over the nicotinamide ring of the cofactor (inhibitor estimated occupancy of 100%, Figure 3C). This pocket is mostly hydrophobic, except for the area above Ala34, being negatively charged through the exposure of the carboxylate moiety of Asp54, belonging to helix α1. The hydrophobic residues lining the catalytic cavity are Ala34 of strand β1, Ile47 on the β2-α1 loop, Met55 and Phe58 of helix α1, Leu90, Pro91, Phe94, and Leu97 on the loop α2-β4, and Ile160 of the β6-α7 loop (Figure

https://doi.org/10.1021/acsinfecdis.4c00113
ACS Infect. Dis. 2024, 10, 2755−2774

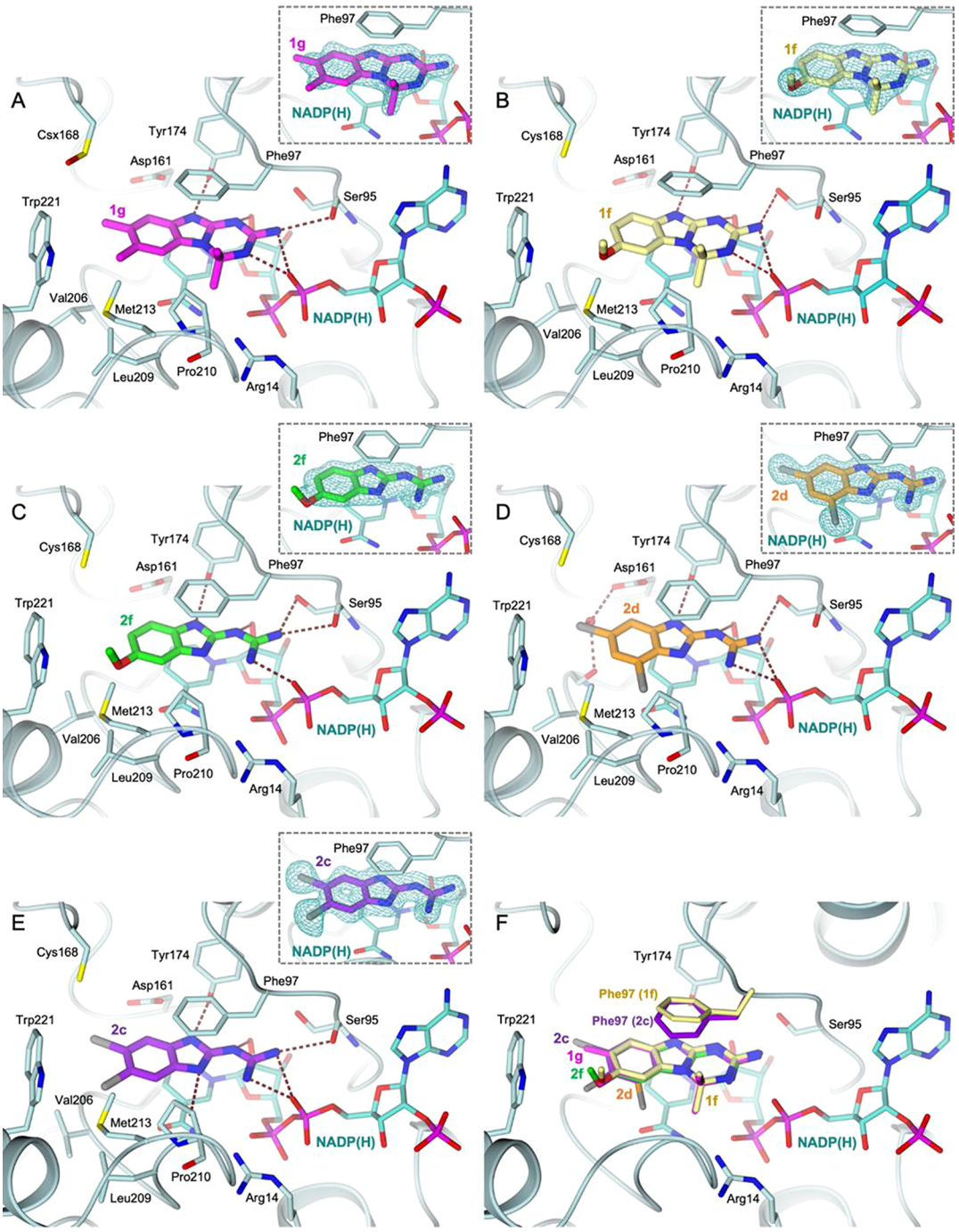

Figure 4. Active site view of *Tb*PTR1 (light cyan car A–E): Active site view of *Tb*PTR1 (light cyan cartoon and carbons) in the ternary complex with the cofactor NADP(H) (in sticks, turquoise carbons) and (A) **1g** (in sticks, magenta carbons), (B) **1f** (in sticks, light yellow carbons), (C) **2f** (in sticks, green carbons), (D) **2d** (in sticks, orange carbons), and (E) **2c** (in sticks, purple carbons). The inhibitor surrounded by the omit map (green mesh contoured at the 2.5σ level) is displayed in the inset of each panel. (F) Structural comparison among the binding modes of compounds **1g** (in sticks, magenta carbons), **1f** (in sticks, light yellow carbons), **2f** (in sticks, green carbons), **2d** (in sticks, orange carbons), and **2c** (in sticks, purple carbons) within the *Tb*PTR1 active site (light cyan cartoon and carbons). The comparison highlights the slight opening of Phe97 in the complexes with the tricyclic compounds **1g** and **1f** (in yellow). This rotation is required to accommodate the bulkier substituents on their dihydrotriazine rings, distorting the peculiar π-sandwich with the cofactor nicotinamide. On the other hand, in the complexes with **2c**, **2d**, and **2f**, Phe97 (in purple) is parallel to the guanidino benzimidazole moiety of the inhibitors and the NADP(H) nicotinamide. In all panels, oxygen atoms are colored red, nitrogen blue, sulfur yellow and phosphorus magenta. Water molecules are shown as red spheres (arbitrary radius) and H-bonds as tan dashed lines.

3C). Among these residues, Phe58 plays a key role in aligning the substrate inside the cavity and stacking with it through its aromatic ring. This interaction is also entailed by **1g**, which exploits its benzimidazole rings to form $\pi-\pi$ stacking with Phe58. The cofactor nicotinamide is located on the opposite side of the benzimidazole rings, to a distance of ~3.5 Å. The aromatic systems of **1g** and the cofactor form an angle of ~80°, generating a distorted T-shaped interaction. Inside the cavity,

https://doi.org/10.1021/acsinfecdis.4c00113
ACS Infect. Dis. 2024, 10, 2755–2774

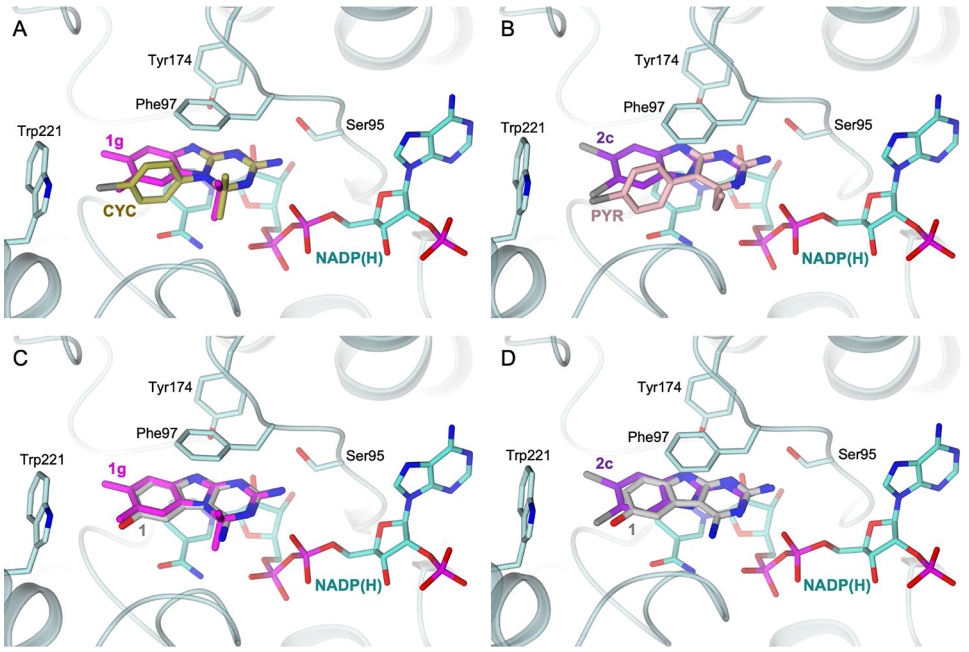

Figure 5. Active site view of the superimposition between the structure of *Tb*PTR1 (light cyan cartoon and carbons) in complex with NADP(H) (in sticks, turquoise carbons) and (A) **1g** (in sticks, magenta carbons) and Cyc (in sticks, gold carbons; PDB id 6HNC[25]); (B) **2c** (in sticks, purple carbons) and Pyr (in sticks, pink carbons; PDB id 7OPJ[27]); (C) **1g** (in sticks, magenta carbons) and the tricyclic inhibitor PI (1, in sticks, gray carbons; PDB id 6TBX[21]); (D) **2c** (in sticks, purple carbons) and the tricyclic inhibitor PI (1, in sticks, gray carbons; PDB id 6TBX[21]). In all panels, oxygen atoms are colored red, nitrogen blue, sulfur yellow, and phosphorus magenta.

1g entails a network of van der Waals interactions with Ala34, Ile47, Met55, Thr86, and Leu90. The inhibitor is further stabilized by the H-bonds taken by its nitrogen N(3), which donates to Asp54, and by the C(2) amine moiety, which donates to both the Val33 backbone carbonyl and Thr185 hydroxyl groups (Figure 3C).

The comparison with the complex *Tb*DHFR-NADP(H)-Pyr (PDB id 3QFX) shows both inhibitors occupying the same area of the active site (Figure 3D).[26] The position of the **1g** dihydrotriazine ring matches the Pyr pyrimidine moiety, sharing the interactions with Asp54 and Thr185. The cofactor nicotinamide is slightly shifted in the complex with Pyr, reasonably because of the hindrance generated by its *p*-Cl-phenyl moiety which is rotated by 90° on the pyrimidine plane (Figure 3D).

X-ray Crystallography of the Complexes of *Tb*PTR1 with Inhibitors and the NADP(H) Cofactor. The structure of *Tb*PTR1 was solved in complex with the cofactor NADP(H) and five inhibitors, **1f**, **1g**, **2c**, **2d**, and **2f** (Tables S1 and S2); the overall structure of *Tb*PTR1 is described in the SI. The tricyclic compounds **1f** and **1g** were crystallized with *Tb*PTR1 and their structures were determined to 1.70 and 1.71 Å resolution, respectively (Tables S1 and S2). In the complex with **1g**, the inhibitor binds inside all four catalytic cavities of the *Tb*PTR1 tetramer, although to a low extent in subunit B (estimated to 50%; inhibitor and cofactor estimated occupancies are summarized in Table S3). On the other hand, three chains of the enzyme tetramer are populated in the complex with **1f**, whereas in the fourth, only the cofactor is observed (Table S3). The PTR1 substrate, DHB, is replaced by the compounds; therefore, these structural bases support a competitive inhibition pattern with respect to DHB.

In both complexes, the tricyclic inhibitors occupy the substrate-binding pocket, being stacked in the peculiar NADP(H) nicotinamide-Phe97 π-sandwich (Figure 4A,B). The compounds are also stabilized inside the pocket by a tight network of conserved H-bonds entailed with the cofactor and surrounding residues. The nitrogen N(1) of the dihydrotriazine ring receives a H-bond from the NADP(H) ribose hydroxyl, whereas the nitrogen N(3) donates a H-bond to the cofactor β-phosphate. The amine moiety in position 2 of the same ring donates a first H-bond to the same cofactor phosphate, and a second is entailed with the Ser95 hydroxyl. A further H-bond is formed with the Tyr174 hydroxyl, which donates a H-bond to the benzimidazole nitrogen N(10). The inhibitors are characterized by peculiar substituents on the terminal benzene ring, being two methyl groups in positions 7 and 8 of **1g** (Figure 4A) and a 7-methoxy group in **1f** (Figure 4B). The methyl group in position 8 of **1g** is directed toward the Trp221 indole, forming van der Waals interaction with it (Figure 4A). The substituents in position 7 of both inhibitors are accommodated inside the hydrophobic region lined by Val206, Leu209, Pro210, Met213, and Trp221 (Figure 4A,B).

Three additional bicyclic compounds, **2c**, **2d**, and **2f**, were crystallized in complex with *Tb*PTR1 and the structures were determined to medium-high resolution (1.86, 1.49, and 1.70 Å, respectively; Tables S1 and S2). In the three complexes, the inhibitor populates the active site of all enzyme subunits within the *Tb*PTR1 tetramer (Table S3), showing conserved binding modes and interactions inside the catalytic cavities (Figure 4C−E). The shared guanidino benzimidazole moiety of the compounds occupies the biopterin binding pocket, positioning the five-membered ring inside the NADP(H) nicotinamide-Phe97 π-sandwich. The benzimidazole nitrogen N(1) donates a hydrogen bond to the Tyr174 hydroxyl. Furthermore, the guanidinium moiety in position 2 donates four H-bonds to Ser95 and the NADP(H) β-phosphate and ribose hydroxyl (Figure 4C−E). These interactions are shared with the tricyclic

https://doi.org/10.1021/acsinfecdis.4c00113
ACS Infect. Dis. 2024, 10, 2755−2774

inhibitors **1g** and **1f**, having the terminal dihydrotriazine ring that mimics the binding mode of the guanidium moiety (Figure 4A,B). Compounds **2c**, **2d**, and **2f** differ in the substituents on the terminal benzene ring. A 5-methoxy is present in compound **2f** (Figure 4C), whereas the inhibitors **2c** and **2d** have two chlorines in positions 5,6 and 4,6, respectively (Figure 4D,E). The substituent in position 5, either the chlorine in **2c** or the methoxy in **2f**, is accommodated inside the hydrophobic pocket lined by Val206, Leu209, Pro210, Met213, and Trp221 (Figure 4C,E). The shared 6-chlorine of **2c** and **2d** is directed toward the nearby area defined by Asp161, Met163, Cys168, and Trp221 (Figure 4D,E). In the complex with **2d**, water-mediated interactions are formed between this chlorine and both the Asp161 carboxylate and the Gly205 back carbonyl (Figure 4D). On the other hand, the second chlorine substituent in position 4 of **2d** faces Leu209 and Pro210, belonging to the substrate-binding loop.

The comparison among the complexes highlights that all compounds populate the active site with analogous binding modes, forming shared interactions with Ser97, Tyr174, and the cofactor. The variable portions of the inhibitors mainly entail hydrophobic interactions inside the cavity resulting in similar K_i values (ranging from 3.23 to 9.15 μM). The cavity configuration is tightly conserved upon inhibitor binding, except for a slight opening of Phe97 in the complexes with tricyclic compounds **1f** and **1g** (Figure 4F). Indeed, the phenyl ring of Phe97 is rotated by ∼30°, accommodating the bulky dimethyl substituents on the dihydrotriazine rings of **1f** and **1g**, and distorting the peculiar π-sandwich with the cofactor nicotinamide.

The binding mode of the compounds was compared to those formerly described for Cyc (PDB id 6HNC) (Figure 5A) and Pyr (PDB id 7OPJ) (Figure 5B).[25,27] Cyc shares with the tricyclic compounds **1f** and **1g** the terminal dihydrotriazine ring, acting as an anchoring moiety inside the substrate-binding pocket (Figure 5A). The binding mode of this moiety inside the cavity is remarkably similar, forming also conserved interactions with the cofactor and Ser95. An additional amine substituent is present on the dihydrotriazine ring of Cyc, mimicking the same interaction with Tyr174 formed by the benzimidazole nitrogen N(10) of tricyclic compounds **1g** and **1f**. A more planar geometry characterizes the terminal guanidinium group of bicyclic compounds **2c**, **2d**, and **2f**, better mimicking the planar triazine ring of Pyr (Figure 5B). The comparison among their complexes enlightens that they share the same interactions inside the substrate-binding pocket, involving the cofactor, Ser95, and Tyr174. On the opposite side of the cavity, Pyr and Cyc form a peculiar halogen bond with Trp221, through the *p*-chlorine on their phenyl moiety (Figure 5A,B). Despite the presence of either 5,6-diCl or 4,6-diCl substituents on the **2c** and **2d** benzimidazole rings, the inhibitors are not correctly aligned with Trp221, preventing the formation of the same type of interaction.

We formerly reported the development of a tricyclic-based inhibitor, named compound PI (PDB id 6TBX[21]) (Figure 1 and 5C,D). The comparison with the binding modes of tricyclic (**1g** in Figure 5C) and bicyclic compounds (**2c** in Figure 5C,D) shows conserved orientations, highlighting once again the importance of the interactions entailed with the cofactor, Ser95, and Tyr174, acting as the main anchoring points inside the cavity (Figure 5C,D).

In Vitro Antiparasitic Activity. The compounds were initially benchmarked for their cytotoxicity against the monocytic THP-1 cell line of human leukemia (Table 3). Excepting the 7,8-dichloro-2-aminotriazino benzimidazole **1c**, which produced certain toxicity (CC_{50} > 50 μM), all the compounds showed a high margin of safety (CC_{50} = 95.3 to >100 μM). Hence, they were evaluated for their in vitro antiparasitic activities against the cultured bloodstream form of *T. brucei* and promastigote stage of *L. infantum*, to probe their potential broad-spectrum antitrypanosomatidic activity.

The compounds were tested at 20 μM against *T. brucei* and *L. infantum*, and only when the cell growth inhibition was higher than 50%, a dose response experiment was performed to calculate the corresponding EC_{50} values (Table 3). Cyc, Pyr, and MTX were used as antifolate reference drugs; pendamidine (PENT) and miltefosine (MLF) were the positive controls for antitrypanosoma and antileishmanial activity tests, respectively (Table 3).

In the case of *T. brucei*, the activity was evaluated using two media: complete HMI-9 medium, corresponding to a final folate concentration of 9 μM; folate deficiency HMI-9 medium, corresponding to a final folate concentration of about 20 nM, aimed at evaluating the effect of folic acid on the inhibition potency of the compounds. The competitive inhibition mechanism of the molecules was investigated by adding DHF, as a natural substrate of *Tb*DHFR.

The parasite most sensitive to the action of the compounds resulted in *T. brucei* whose growth was affected by 71% of 2-guanidino benzimidazoles (series **2**) which provided EC_{50} values in the range from 2.91 (**2d**) to 18.2 μM (**2e**). The active compounds were monosubstituted at position 5 (**2b**, **2e**), disubstituted at positions 5 and 6 (**2c**, **2g**), or 4 and 6 (**2d**) of the benzimidazole ring with lipophilic groups, both electron-withdrawing (Cl, CF_3) or electron-donating (CH_3). Conversely, the presence of a polar group (5-OCH_3, **2f**) rather than the absence of substituents (**2a**) was associated with the loss of activity (EC_{50} > 20 μM).

In the series of triazino benzimidazoles **1**, only the 7,8-dimethyl derivative (**1g**) was proven to inhibit *T. brucei*, reaching an EC_{50} of 6.63 μM. Collectively, in the standard folate medium, the compounds showed an antiparasitic activity improved or comparable to those of antifolate drugs Pyr and MTX (EC_{50} of 17.3 and 23.3 μM, respectively), even better than that of Cyc (EC_{50} > 80 μM).

In relation to the screening carried out in the folate deficiency medium, the compounds showed no gain in the activity trend, which remained unvaried with respect to folate standard conditions. This supports the concept that these compounds may have a multitargeting activity and do not inhibit only the folate-dependent enzymes, such as DHFR or PTR1.

Differently, for the antifolate reference drugs, the activity ameliorated in the folate deficiency medium, as markedly evidenced by MTX whose EC_{50} enhanced 4300-fold passing from 23.3 μM to 5.4 nM. Such a behavior agreed with previous findings, in which antifolate drugs containing a terminal glutamic acid moiety like MTX and pemetrexed demonstrated the highest potency against *T. brucei* when tested in a medium deficient in folate and/or thymidine. This polar side chain was proposed to be relevant for transport and subsequent increased retention of these folate mimetic inhibitors in the trypanosome after polyglutamylation, a post-translational modification leading to an improved antiparasitic effect. The same did not

https://doi.org/10.1021/acsinfecdis.4c00113
ACS Infect. Dis. 2024, 10, 2755−2774

happen to folate inhibitors Pyr, trimetrexate, and nolatrexed where potency did not change between medium types likely due to the fact that they are more lipophilic and lack the terminal glutamyl moiety.[17] Analogous consideration could be made for the present compounds, for which lipophilicity was predicted through the SwissADME Web site calculating their Log *P* values[39] in comparison to MTX, pemetrexed, Cyc, Pyr, trimetrexate, and nolatrexed. Interestingly, the results, listed in Table S4, confirmed for both series Log *P* values were always higher than those of MTX, and pemetrexed (except for **2a** and **2f**), and comparable to those of the other antifolate drugs.

Finally, most of the compounds did not show an appreciable antiparasitic activity against the promastigote form of *L. infantum* (Table 3) apart from the 2-guanidino derivatives **2d** (EC_{50} = 6.62 μM) and **2c** (EC_{50} = 22.5 μM), surpassing the potency of Cyc (EC_{50} > 80 μM) and Pyr (EC_{50} = 99.2 μM) and well matching that of MLF, which exhibited an EC_{50} of 10.9 μM. Thus, they demonstrated a valuable broad-spectrum antiparasitic activity, by affecting both *Trypanosoma* and *Leishmania* parasites' growth.

CONCLUSIONS

To bring out new opportunities for the treatment of HAT and Leishmaniasis, we uncovered two novel chemotypes starting from the structural analysis of Cyc and Pyr, which were proven to be attractive template molecules targeting the DHFR and PTR1 of *T. brucei*. Accordingly, the amino dihydrotriazine moiety of Cyc was condensed to the benzimidazole nucleus giving the 2-aminotriazino benzimidazoles of series **1**, which demonstrated a nanomolar inhibition of *Tb*DHFR and 2 orders of magnitude lower activity against *Tb*PTR1. The isosteric replacement of the 2-aminotriazine moiety from series **1** delivered the 2-guanidino group in series **2**, as less conformationally constrained analogues, which even improved their performance against *Tb*DHFR reaching the low nanomolar potency range. Outstandingly, the 5,6-dimethyl-2-guanidinobenzimidazole **2g** was found to be the most potent (K_i = 9 nM) and highly selective *Tb*DHFR inhibitor, 6000-fold over *Tb*PTR1 and 394-fold over *h*DHFR. Considering its peculiar selectivity for *Tb*DHFR, **2g** could be valorized in drug combination tests with a potent and selective *Tb*PTR1 inhibitor to yield the synergistic inhibition of the trypanosomatid folate pathway.

However, the pronounced potency against *Tb*DHFR of **2g** and structural analogues (**2b**−**2e**) is not reflected against the whole cells, as the antiparasitic activity ranges in the low micromolar domain and does not vary linearly with enzymatic inhibition potency. This also encompasses the 7,8-dimethyl triazino benzimidazole (**1g**), the only compound of series **1** to be found as active against *T. brucei* parasites (EC_{50} = 6.63 μM). Conceivably, this outcome could be attributed to the modest inhibition of *Tb*PTR1, whereby the compounds do not properly achieve the dual inhibition of both folate enzymes. Although the definition of a single inhibitor motif targeting both enzymes remains elusive, the structural elucidation of *Tb*DHFR and *Tb*PTR1 in complex with the present chemotypes may benefit the design of more promising, or even dual, inhibitors. Since only few cocrystal structures have been released for *Tb*DHFR, the *Tb*DHFR:**1g** complex presented in this study may significantly expand on the knowledge of the bonding interactions mapping for active site inhibition, which can serve the purpose of supporting future design work and provide suggestions for the tailored modification of *Tb*DHFR inhibitors.

The strongly basic dihydrotriazine scaffold of Cyc was previously demonstrated to mainly exist in the protonated form at physiological pH. The Cyc protonated form can be held liable for its poor bioavailability. To overcome this issue, in malaria therapy, Cyc is administered through its better-suited prodrug, proguanil. Conceivably, a similar consideration could be made for the present compounds, incorporating the dihydrotriazine ring of Cyc or an isostere guanidine thereof. Thus, subsequent studies deserve to investigate the pharmacokinetic profile of both series that could have jeopardized them from achieving their intracellular targets. For instance, modification of their pK_a's leading to a less alkaline character should be taken into account to improve their subcellular uptake and distribution, thus reaching lower EC_{50} in vitro. Moreover, the discovery of the 2-guanidino benzimidazoles **2d** and **2c** as potent and broad-spectrum antiprotozoan leads by inhibiting *Trypanosoma* and *Leishmania* parasites may offer the prominent opportunity to affect multiple parasitic diseases, which needs to be further explored.

METHODS

Chemistry. Chemicals and solvents were purchased from Sigma-Aldrich or Zentek (Milan, Italy). Melting points were determined using a Büchi apparatus and are uncorrected. ^{1}H NMR spectra and ^{13}C NMR spectra were recorded using a Jeol instrument at 400 and 101 MHz, respectively; chemical shifts are reported as δ (ppm) and are referenced to DMSO-d6, quintet at 2.5 ppm (^{1}H), septet at 39.5 ppm (^{13}C); *J* in Hz. Elemental analyses were performed on a Flash 2000 CHNS (Thermo Scientific) instrument in the Microanalysis Laboratory of the Department of Pharmacy, University of Genova. NMR spectra of the novel compounds are shown in the Supporting Information. Results of elemental analyses indicated that the purity of all compounds was ≥95%.

Synthesis of 2-Aminotriazino[1,2-*a*]benzimidazoles 1a−g. A mixture of the proper 2-guanidinobenzimidazole of series 2 (5.7 mmol) and piperidine (2.9 mmol) dissolved in 5 mL of acetone was heated at 70 °C for 7 h. The reaction mixture was then concentrated under vacuum and kept cooling to r.t. overnight. The expected product precipitated as a white solid, which was filtered and crystallized from acetone/Et_2O.

*2-Amino-4,4-dimethyl-3,4-dihydrotriazino[1,2-a]-benzimidazole (**1a**).* Yield: 59%. M.p. 284.8−285.6 °C (M.p. 295−296 °C[34]). ^{1}H NMR (400 MHz, DMSO-*d*6): δ 7.71 (s, 1H, NH), 7.35 (d, *J* = 7.7 Hz, 1H, C(6)−H arom.), 7.24 (d, *J* = 7.7 Hz, 1H, C(9)−H arom.), 6.98 (td, *J* = 7.6, 1.2 Hz, 1H, C(7)−H arom.), 6.91 (td, *J* = 7.6, 1.3 Hz, 1H, C(8)-H arom.), 6.36 (s, 2H, NH_2), 1.77 (s, 6H, C(4)-diCH_3). ^{13}C NMR (101 MHz, DMSO-*d*6) δ: 155.21, 153.66, 143.74, 130.67, 120.55, 118.90, 116.08, 109.60, 69.31, 28.50 (2C). Anal. calcd for $C_{11}H_{13}N_5$: C 61.38, H 6.09, N 32.54; found: C 61.31, H 6.12, N 32.30.

*2-Amino-7(8)-chloro-4,4-dimethyl-3,4-diidrotriazino[1,2-a]benzimidazole (**1b**).* Yield: 41%, m.p. 161.2−163 °C. Ratio **1b-I**/**1b-II**: 60% **1b-I** and 40% **1b-II**. ^{1}H NMR (400 MHz, DMSO-*d*6): **1b-I** δ 7.68 (s, 1H, NH), 7.35 (d, *J* = 8.5 Hz, 1H, C(6)−H arom.), 7.23 (d, *J* = 2.1 Hz, 1H, C(9)−H arom.), 6.89 (dd, *J* = 8.5, 2.1 Hz, 1H, C(7)−H arom.), 6.36 (s, 2H, NH_2), 1.74 (s, 6H, C(4)−diCH_3). **1b-II** δ 7.65 (s, 1H, NH), 7.40 (d, *J* = 2.0 Hz, 1H, C(6)−H arom.), 7.20 (d, *J* = 8.4 Hz, 1H, C(9)−H arom.), 6.99 (dd, *J* = 8.3, 2.1 Hz, 1H, C(8)−H

https://doi.org/10.1021/acsinfecdis.4c00113
ACS Infect. Dis. 2024, 10, 2755−2774

arom.), 6.33 (s, 2H, NH_2), 1.75 (s, 6H, C(4)−diCH_3). ^{13}C NMR (101 MHz, DMSO-d6): **1b-I** δ 155.48, 155.08, 145.27, 129.59, 124.97, 118.32, 115.37, 110.43, 69.79, 28.34 (2C); **1b-II** δ 155.36, 154.56, 142.76, 131.43, 122.94, 120.57, 116.86, 109.30, 69.44, 28.30 (2C). Anal. calcd for $C_{11}H_{12}N_5Cl$: C 52.91, H 4.84, N 28.05; found: C 52.89, H 5.16, N 28.09.

*2-Amino-7,8-dichloro-4,4-dimethyl-3,4-dihydrotriazino-[1,2-a]benzimidazole (**1c**).* Yield: 56%. M.p. 285.1−285.9 °C. ^{1}H NMR (400 MHz, DMSO-d6): δ 7.73 (s, 1H, NH), 7.59 (s, 1H, C(6)−H arom.), 7.40 (s, 1H, C(9)−H arom.), 6.43 (s, 2H, NH_2), 1.75 (s, 6H, C(4)−diCH_3). ^{13}C NMR (101 MHz, DMSO-d6) δ: 155.75, 155.62, 144.11, 130.42, 122.90, 120.39, 116.52, 110.52, 69.58, 28.17 (2C). Anal. calcd for $C_{11}H_{11}N_5Cl_2$: C 46.50, H 3.90, N 24.65; found: C 46.43, H 4.00, N 24.30.

*2-Amino-7,9-dichloro-4,4-dimethyl-3,4-dihydrotriazino-[1,2-a]benzimidazole (**1d**).* Yield: 89%, m.p. 283.2−283.7 °C. ^{1}H NMR (400 MHz, DMSO-d6): δ 7.86 (s, 1H, NH), 7.41 (d, J = 1.8 Hz, 1H, C(6)−H arom.), 7.11 (d, J = 1.8 Hz, 1H, C(8)−H arom.), 6.46 (s, 2H, NH_2), 1.74 (s, 6H, C(4)−diCH_3).^{13}C (101 MHz, DMSO-*d6*): δ 155.64, 155.10, 139.97, 132.07, 122.73, 120.11, 119.97, 108.39, 69.74, 28.21 (2C). Anal. calcd for $C_{11}H_{11}N_5Cl_2$: C 46.50, H 3.90, N 24,65; found: C 46.68, H 3.71, N 24,71.

*2-Amino-7(8)-trifluoromethyl-4,4-dimethyl-3,4-dihydrotriazino[1,2-a]benzimidazole (**1e**).* Yield: 20%, m.p. 259−261 °C. Ratio **1e-I**/**1e-II**: 60% **1e-I** and 40% **1e-II**. ^{1}H NMR (400 MHz, DMSO-d6): **1e-I** δ 7.78 (s, 1H, NH), 7.53 (d, J = 8.3 Hz, 1H, C(6)−H arom.), 7.50 (s, 1H, C(9)−H arom.), 7.20 (dd, J = 8.5, 2.1 Hz, 1H, C(7)−H arom.), 6.43 (s, 2H, NH_2), 1.79 (s, 6H, C(4)−diCH_3); **1e-II** δ 7.80 (s, 1H, NH), 7.57 (s, 1H, C(6)−H arom.), 7.36 (d, J = 8.2 Hz, 1H, C(9)−H arom.), 7.30 (dd, J = 8.4, 2.0 Hz, 1H, C(8)−H arom.), 6.47 (s, 2H, NH_2), 1.79 (s, 6H, C(4)−diCH_3). ^{13}C (101 MHz, DMSO-d6): **1e-I** δ 155.77, 155.58, 143.82, 133.28, 125.31 (d, $^1J_{CF}$ = 272.7 Hz), 121.42 (q, $^2J_{CF}$ = 31.2 Hz), 115.47 (d, $^3J_{CF}$ = 3.8 Hz), 112.41 (d, $^3J_{CF}$ = 3.7 Hz), 109.71, 69.59, 28.38 (2C); **1e-II** δ 156.18, 155.50, 147.03, 130.36, 125.44 (d, $^1J_{CF}$ = 272.7 Hz, CF_3), 118.92 (q, $^2J_{CF}$ = 31.5 Hz), 117.77 (d, $^3J_{CF}$ = 3.6 Hz), 115.91, 106.10 (d, $^3J_{CF}$ = 3.7 Hz), 69.64, 28.32 (2C). Anal. calcd for $C_{12}H_{12}F_3N_5$: C 50.88, H 4.74, N 24.72; found: C 50.82, H 4.53, N 24.75.

*2-Amino-7(8)-methoxy-4,4-dimethyl-3,4-dihydrotriazino-[1,2-a]benzimidazole (**1f**).* Yield: 21%. M.p. 264−266 °C. Ratio **1f-I**/**1f-II**: 64% **1f-I** and 36% **1f-II**. ^{1}H NMR (400 MHz, DMSO-*d6*): **1f-I** δ 7.63 (s, 1H, NH), 7.21 (d, J = 8.6 Hz, 1H, C(6)−H arom.), 6.82 (d, J = 2.5 Hz, 1H, C(9)−H arom.), 6.52 (dd, J = 8.7, 2.5 Hz, 1H, C(7)−H arom.), 6.27 (s, 2H, NH_2), 3,72 (s, 3H, C(8)−OCH_3), 1.72 (s, 6H, C(4)−diCH_3); **1f-II** δ 7.59 (s, 1H, NH), 7.13 (d, J = 8.6 Hz, 1H, C(9)−H arom.), 6.88 (d, J = 2.4 Hz, 1H, C(6)−H arom.), 6.63 (dd, J = 8.6, 2.4 Hz, 1H, C(8)−H arom.), 6.22 (s, 2H, NH_2), 3,75 (s, 3H, C(7)−OCH_3), 1.75 (s, 6H, C(4)−diCH_3). ^{13}C NMR (101 MHz, DMSO-d6): **1f-I** δ 155.14, 154.70, 153.48, 144.86, 125.16, 109.58, 106.42, 100.77, 69.21, 55.32, 28.43 (2C); **1f-II** δ 154.81, 154.38, 153.07, 137.97, 131.09, 116.15, 107.56, 95.90, 69.24, 55.72, 28.43 (2C). Anal. calcd for $C_{12}H_{15}N_5O$: C 58.76, H 6.16, N 28.55; found: C 59.03, H 6.22, N 28.93.

*2-Amino-4,4,7,8-tetramethyl-3,4-dihydrotriazino[1,2-a]-benzimidazole (**1g**).* Yield: 40%. M.p. 266.5−268.5 °C. ^{1}H NMR (400 MHz, DMSO-d6): δ 7.54 (s, 1H, NH), 7.12 (s, 1H, C(6)−H arom.), 7.02 (s, 1H, C(9)−H arom.), 6.16 (s, 1H, NH_2), 2.25 (s, 3H, C(8)−CH_3), 2.21 (s, 3H, C(7)−CH_3), 1.73 (s, 6H, C(4)−diCH_3). ^{13}C NMR (101 MHz, DMSO-d6) δ 154.91, 153.07, 142.09, 129.06, 128.09, 126.73, 116.89, 110.33, 69.14, 28.49 (2C), 19.90, 19.75. Anal. calcd for $C_{13}H_{17}N_5$: C 64.17, H 7.04, N 28.78; found: C 64.22, H 7.32, N 28.50.

Synthesis of 2-Guanidino Benzimidazoles 2a−g. The properly substituted 1,2-phenylendiamine (1,4 mmol) and dicyandiamide (1,4 mmol) were dissolved in 5 mL of H_2O, and 0.23 mL (1,4 mmol) of conc. HCl. The mixture was heated to reflux for 6h with stirring. After cooling to rt, the solution was alkalinized with 6 M NaOH inducing the precipitation of an amorphous solid, which was either crystallized from Et_2O (**2a**) or purified by CC (SiO_2/Et_2O + 10% MeOH) (**2b−2g**), to afford the final product. Compounds **2b**, **2c**, and **2e** were converted to their respective hydrochloride salts by adding HCl 1N (ethanolic solution) to perform elemental analysis.

*2-Guanidinobenzimidazole (**2a**).* Yield: 59%. M.p. 237−240 °C (m.p. 243−244 °C[33]). ^{1}H NMR (400 MHz, DMSO-d6): δ 10.95 (br s, 1H, benzimidazole exchangeable NH), 7.33−6.46 (br s, 4H, 2NH, and NH_2 signals superimposed to H arom.), 7.18−7.12 (m, 2H, H arom.), 6.93−6.88 (m, 2H, H arom.), 3.35 (br s, 1H, NH signal partially superimposed to the H_2O peak). ^{13}C NMR (101 MHz, DMSO-d6): δ 158.96, 158.72, 133.60 (2C), 119.36 (2C), 111.91 (2C). Anal. calcd for $C_8H_9N_5$: C 54.85, H 5.18, N 39.98; found: C 54.51, H 5.40, N 39.94.

*5(6)-Chloro-2-guanidinobenzimidazole (**2b**).* Yield: 40%. M.p. 208−211 °C (M.p. 207 °C[33]). ^{1}H NMR (400 MHz, DMSO-*d6*): δ 11.12 (br s, 1H, benzimidazole exchangeable NH), 7.20−6.50 (br s, 3H, NH and NH_2 signals superimposed to H arom.), 7.15 (s, 1H, H arom.), 7.11 (d, J = 8.3 Hz, 1H, H arom.), 6.90 (dd, J = 8.3, 2.1 Hz, 1H, H arom.), 3.38 (br s, 1H, NH signal partially superimposed to the H_2O peak). ^{13}C NMR (101 MHz, DMSO-*d6*) δ: 160.16, 158.99, 142.76, 133.63, 123.54, 119.06, 113.84, 109.77. Anal. calcd for $C_8H_8ClN_5 \cdot 2HCl$: C 34.01, H 3.57, N 24.79; found: C 34.06, H 3.45, N 24.88.

*5,6-Dichloro-2-guanidinobenzimidazole (**2c**).* Yield: 70%. M.p. 236−240 °C (M.p. 244 °C[33]). ^{1}H NMR (400 MHz, DMSO-*d6*): δ 11.21 (s, 1H, benzimidazole exchangeable NH), 7.29 (s, 2H, H arom.), 6.97 (br s, 3H, NH + NH_2), 3.34 (br s, 1H, NH). ^{13}C NMR (101 MHz, DMSO-*d6*): δ 161.01, 159.20, 121.09 (2C), 114.13 (2C), 110.33 (2C). Anal. calcd for $C_8H_7Cl_2N_5 \cdot HCl$: C 34.25, H 2.87, N 24.96; found: C 34.31, H 3.10, N 24.54.

*4,6-Dichloro-2-guanidinobenzimidazole (**2d**).* Yield: 40%. M.p. 244−245.5 °C. ^{1}H NMR (400 MHz, DMSO-*d6*): δ 11.60 (s, 1H, benzimidazole exchangeable NH), 7.17 (br s, 3H, NH + NH_2), 7.12 (d, J = 1.9 Hz, 1H, H arom.), 7.05 (d, J = 1.9 Hz, 1H, H arom.). 3.34 (br s, 1H, NH). ^{13}C NMR (101 MHz, DMSO-*d6*): δ 159.29, 158.88, 135.72, 131.13, 123.42, 119.00, 115.24, 109.11. Anal. calcd for $C_8H_7Cl_2N_5$: C 39.37, H 2.89, N 28.69; found: C 39.44, H 3.02, N 28.38.

*5(6)-Trifluoromethyl-2-guanidinobenzimidazole (**2e**).* Yield 38%. M.p. 200−203 °C. ^{1}H NMR (400 MHz, DMSO-d6): δ 8.38 (br s, 4H, 2NH + NH_2), 7.72 (s, 1H, H arom.), 7.59 (d, J = 8.3 Hz, 1H, H arom.), 7.49 (dd, J = 8.5, 1.8 Hz, 1H, H arom.). ^{13}C NMR (101 MHz, DMSO-*d6*): δ 156.46, 149.15, 137.33, 134.68, 124.88 (q, $^1J_{CF}$ = 271.5 Hz), 122.61 (q, $^2J_{CF}$ = 31.5 Hz), 118.96 (d, $^3J_{CF}$ = 3.9 Hz), 113.70, 110.54. Anal. calcd for $C_9H_8F_3N_5 \cdot HCl$: C 38.65, H 3.24, N 25.04; found: C 38.41, H 3.21, N 25.01.

https://doi.org/10.1021/acsinfecdis.4c00113
ACS Infect. Dis. 2024, 10, 2755−2774

*5(6)-Methoxy-2-guanidinobenzimidazole (**2f**).* Yield: 36%. M.p. 201.7−202.7 °C. ^{1}H NMR (400 MHz, DMSO-d6): δ 10.88 (br s, 1H, benzimidazole exchangeable NH), 7.20−6.26 (br s, 3H, NH and NH_2 signals superimposed to H arom.), 7.03 (d, J = 8.4 Hz, 1H, H arom.), 6.74 (d, J = 2.4 Hz, 1H, H arom.), 6.53 (dd, J = 8.5, 2.5 Hz, 1H, H arom.), 3.71 (s, 3H, C(5)−OCH_3), 3.34 (br s, 1H, NH signal partially superimposed to the H_2O peak). ^{13}C NMR (101 MHz, DMSO-*d*6): δ 158.84, 158.44, 154.02, 133.97, 111.54, 107.05, 96.72, 55.35. Anal. calcd for $C_9H_{11}N_5O$: C 52.67, H 5.40, N 34.13; found: C 52.63, H 5.45, N 34.43.

*5,6-Dimethyl-2-guanidinobenzimidazole (**2g**).* Yield: 65%. M.p. 167.2−170 °C (m.p. 191 °C[33]). ^{1}H NMR (400 MHz, DMSO-*d*6): δ 10.84 (s, 1H, benzimidazole exchangeable NH), 6.94 (s, 2H, H arom.), 6.84 (br s, 3H, NH + NH_2 signals partially superimposed to H arom.), 3.35 (br s, 1H, NH), 2.22 (s, 6H, C(5)−CH_3 and C(6)−CH_3). ^{13}C NMR (101 MHz, DMSO-*d*6): δ 158.98, 158.57, 135.81 (2C), 127.57 (2C), 112.97 (2C), 20.39 (2C). Anal. calcd for $C_{10}H_{13}N_5$: C 59.10, H 6.45, N 34.46; found: C 59.16, H 6.74, N 34.73.

HPLC Chromatography. The product was analyzed using an Agilent 1100 HPLC-MSD Ion Trap XCT system equipped with an electrospray ion source (HPLC-ESI-MS/MS) (Agilent Technologies, Santa Clara, CA, USA).

Chromatographic analyses were performed using a Waters Symmetry 300 C_{18} column (particle size 3,5 μm−150 × 1 mm) at room temperature and gradient elution with a binary solution (eluent A: H_2O/HCOOH 0.1% v/v, eluent B: ACN/HCOOH 0.05% v/v). The analysis started with 0 of B (t_0); then, B was increased to 100% (from t_0 to t_1 = 30 min), then kept at 100% (from t_1 to t_2 = 35 min), and finally returned to 0% of eluent B in 7 min. The flow rate was 300 μL/min and the injection volume was 8 μL. UV detection was monitored at 254. Mass spectra were acquired in positive ion mode, in the 50−500 m/z range and ion charged control with a target ion value of 50,000 and an accumulation time of 300 ms. A capillary voltage of 3000 V, nebulizer pressure of 10 psi, drying gas of 5 L/min, dry temperature of 325 °C, and rolling averages of 3 (averages: 5) were the parameters set for the MS detection.

Protein Production for X-ray Crystallography and Enzymatic Characterization. *Recombinant TbDHFR-TS and TbDHFR. 6xHis-TbDHFR-TS* (EC:1.5.1.3) was produced in *E. coli* ArcticExpress (DE3) cells and purified by exploiting the N-terminal His^6-tag, according to established protocols.[40]

The synthetic gene encoding for *Tb*DHFR, optimized for *E. coli* expression, and cloned in the pET-15b expression vector within the NdeI-BamHI restriction sites (pET15b−*Tb*DHFR plasmid), was purchased from GenScript. Through this plasmid vector, the target protein is produced as a thrombin cleavable His^6-tag protein (HT-*Tb*DHFR), allowing its purification through the IMAC technique. The pET15b−*Tb*DHFR plasmid was used to heath-shock transform chemically competent *E. coli* ArcticExpress (DE3) cells. Bacteria were cultured at 20 °C in the ZYP-5052 autoinduction medium[41] (supplemented with 100 mg/L ampicillin) for 48 h under vigorous aeration (220 rpm). Cells, harvested by centrifugation (3500 g, 15 min, 8 °C), were resuspended in buffer A (25 mM KP_i pH 7.4 and 0.15 M NaCl), supplemented with lysozyme (0.5 mg/mL) and 0.1 mM phenylmethylsulfonyl fluoride (PMSF), and disrupted by sonication after 30−60 min of incubation on ice. The supernatant of the resulting crude extract, including the target protein, was clarified by centrifugation (14,000g, 1 h, 8 °C). HT-*Tb*DHFR was purified by nickel-affinity chromatography on a HisTrap HP 5 mL column (GE-Healthcare), performing the elution from the matrix using buffer A supplemented with 250−500 mM imidazole. Collected fractions including the target protein, identified by SDS-PAGE analysis, were combined and subjected to dialysis in buffer A at 8 °C (dialysis membrane cutoff 14 kDa). The His^6-tag was cleaved during dialysis by adding thrombin protease (5U/$mg_{HT\text{-}TbDHFR}$) to the target sample. The resulting mature *Tb*DHFR was separated by a second stage of nickel-affinity chromatography and finally purified through size-exclusion chromatography on a HiLoad 16/600 Superdex 75pg (GE-Healthcare), equilibrated in buffer A. The high purity of the final sample of mature *Tb*DHFR was confirmed by SDS-PAGE analysis (purity >98%) and high-resolution MS (aa 244, M.W. 26,549.71 Da), and the yield was established to be ∼9 mg/$L_{cell\ culture}$. Enzymatic activity of each protein was calculated with kinetics direct assay and spectrophotometric readout as reported in the literature.[27,40] Measured parameters for *Tb*DHFR-TS for the reductase domain were k_{cat} 1.07 ± 0.06 s^{-1}, K_M(DHF) 4.88 ± 1.15 μM, and K_M(NADPH) 23.01 ± 5.12 μM.[27,40]

Recombinant LmDHFR-TS. Recombinant *Lm*DHFR-TS (EC:1.5.1.3) was cloned in the pET-15b(TEV) vector and expressed in the*E. coli* strain ArcticExpress (DE3). Bacterial culture was grown at 30 °C in ZYP-5052 autoinduction medium (supplemented with ampicillin 100 mg/L) to $OD_{600\ nm}$ value of about 1, and then cell growth was continued for 60 h at 12 °C under vigorous aeration. Cells, harvested by centrifugation (3500g, 15 min, 8 °C), were resuspended in buffer A (50 mM sodium citrate pH 5.5 and 0.25 M NaCl), supplemented with lysozyme (0.5 mg/mL) and 0.1 mM PMSF, and disrupted by sonication after 30−60 min of incubation on ice. The enzyme was purified by nickel-affinity chromatography on a HisTrap FF 5 mL column (GE-Healthcare), performing the elution from the matrix using buffer A, supplemented with 250−500 mM imidazole. Collected fractions including the target proteins, identified by SDS-PAGE analysis, were combined and dialyzed overnight in buffer A at 8 °C. The resulting protein sample was further purified on a gel filtration column (HiLoad 16/600 Superdex 200pg, GE Healthcare) equilibrated in buffer A. The high purity of the final sample was confirmed by SDS-PAGE (≥98%) and MS (aa 541, M.W. 61,094.19 Da), and the yield was established to be ∼20 mg/L_{cell}. Enzymatic activity of each protein was calculated with kinetics direct assay and spectrophotometric readout as reported in the literature.[27,40] Enzymatic measured parameters for *Lm*DHFR were k_{cat} 13.02 ± 1.12 s^{-1}, K_M(DHF) 4.56 ± 0.98 μM, and K_M(NADPH) 11.1 ± 1.25 μM. These data agree with previous literature studies.[27,42,43]

Recombinant TcDHFR-TS. The synthetic gene encoding for *Tc*DHFR-TS, optimized for *E. coli* expression and cloned in the pET-11a expression vector, was purchased from GenScript. The plasmid vector was introduced by thermal shock in the *E. coli* strain BL21(DE3). The bacterial culture was grown at 37 °C in LB medium supplemented with 100 mg/L ampicillin. Protein over-expression was induced with 1 mM IPTG when the cell density reached an $OD_{600\ nm}$ of 0.6−0.8 and cell growth was continued at 25 °C for 16 h. Cells, harvested by centrifugation (3500 g, 15 min, 8 °C), were resuspended in buffer A (50 mM Tris-HCl pH 7.2), supplemented with

https://doi.org/10.1021/acsinfecdis.4c00113
ACS Infect. Dis. 2024, 10, 2755−2774

lysozyme (0.5 mg/mL) and 0.1 mM PMSF, and disrupted by sonication. The enzyme was purifed by anion exchange chromatography (Mono Q HR 16/10 column, 20 mL) and proteins were eluted using a linear gradient of sodium chloride (0-500 mM). Fractions containing *Tc*DHFR-TS were identified by SDS-PAGE, pooled and concentrated. The resulting sample was purified by size-exclusion chromatography on a HiLoad 16/600 Superdex 200pg column (GE-Healthcare), equilibrated with 25 mM Tris pH 7.2, 250 mM NaCl, and 10 mM DTT. The target protein was further purified through a second anion-exchange DEAE Sepharose FF column (GE-Healthcare), using a linear gradient of sodium chloride (0−250 mM) in 25 mM Tris pH 7.2, supplemented with 10 mM DTT. The high purity of the final sample of mature proteins was confirmed by SDS-PAGE (≥98%) and MS (aa 521, M.W. 58,853.26 Da, per monomer), and the yield was established to be ∼15 mg/L_{cell}. Enzymatic activity was calculated with kinetics direct assay and spectrophotometric readout as reported in the literature.[27,40] Measured parameters for *Tc*DHFR-TS were k_{cat} 28.01 ± 2.22 s^{-1}, K_M(DHF) 2.35 ± 0.24 μM, and K_M(NADPH) 8.12 ± 0.84 μM, which agree with previous findings.[43]

Recombinant TbPTR1. *6xHis-Tb*PTR1 (EC:1.5.1.33) was produced in *E. coli* BL21(DE3) cells and purified by exploiting the N-terminal His^6-tag (HT-*Tb*PTR1), according to established protocols.[40] The synthetic gene encoding for *Tb*PTR1 is cloned in the pET-15b vector. The pET15b−*Tb*PTR1 plasmid was used to heath-shock transform chemically competent *E. coli* BL21(DE3) cells. Bacteria were cultured at 30 °C in Luria−Bertani broth supplemented with 100 mg/L ampicillin under vigorous aeration (220 rpm) and induced with 1 mM IPTG at 30 °C overnight. Cells, harvested by centrifugation (3500 g, 15 min, 8 °C), were resuspended in 50 mM Tris HCl, 250 NaCl, pH 7.5, supplemented with lysozyme (0.5 mg/mL) and 0.1 mM PMSF, and disrupted by sonication after 30−60 min of incubation on ice. The supernatant of the resulting crude extract, including the target protein, was clarified by centrifugation (14,000*g*, 1 h, 8 °C). HT-*Tb*PTR1 was purified by nickel-affinity chromatography on a HisTrap HP 5 mL column (GE-Healthcare), performing the elution from the matrix using buffer A supplemented with 250−500 mM imidazole. Collected fractions including the target protein, identified by SDS-PAGE analysis, were combined and subjected to dialysis in buffer A at 8 °C (dialysis membrane cutoff 14 kDa). The high purity of the final sample of HT-*Tb*PTR1 was confirmed by SDS-PAGE analysis and high-resolution MS (aa 289, 30,764.99 Da, per monomer), and the yield was established to be ∼9 mg/$L_{cell\ culture}$. Enzymatic activity was calculated with kinetics direct assay and spectrophotometric readout as reported in the literature.[27,40] Kinetic parameters for *Tb*PTR1 were k_{cat} 0.74 ± 0.07 s^{-1}, K_M(BH2 or DHB) 5.62 ± 0.64 μM, and K_M(NADPH) 12.30 ± 0.31 μM.[40]

Recombinant hDHFR. *6xHis-h*DHFR (EC:1.5.1.3) was produced in *E. coli* strain ArcticExpress(DE3) cells. The synthetic gene encoding for *h*DHFR, optimized for *E. coli* expression and cloned in the pET15b expression vector within the NdeI-*Bam*HI restriction sites, was purchased from GenScript. Through this plasmid vector, the target protein is produced as a thrombin cleavable His^6-tag protein. The pET15b−*h*DHFR plasmid was used to heath-shock transform chemically competent *E. coli* ArcticExpress (DE3) cells. Bacterial culture was grown at 30 °C in ZYP-5052 auto-induction medium (supplemented with ampicillin 100 mg/L) to $OD_{600\ nm}$ value of about 1, and then cell growth was continued for 60 h at 12 °C under vigorous aeration. Cells, harvested by centrifugation (3500*g*, 15 min, 8 °C), were resuspended in buffer A (25 mM KH_2PO_4 pH 7 and 50 mM NaCl), supplemented with lysozyme (0.5 mg/mL) and 0.1 mM PMSF and disrupted by sonication after 30−60 min of incubation on ice. HT-*h*DHFR was purified by nickel-affinity chromatography on a HisTrap HP 5 mL column (GE-Healthcare). The target protein was eluted using buffer A supplemented with 250 mM imidazole. Collected fractions containing HT-*h*DHFR were combined with thrombin protease (3 units/$mg_{HT\text{-}hDHFR}$) and dialyzed overnight in buffer A (membrane cutoff 14 kDa) at 8 °C. The resulting mature *h*DHFR was separated by a second stage of nickel-affinity chromatography and finally purified through size-exclusion chromatography on a HiLoad 16/600 Superdex 75pg (GE-Healthcare), equilibrated in buffer A. The high purity of the final sample of mature *h*DHFR was confirmed by SDS-PAGE (≥98%) and high-resolution MS (aa 190, M.W. 21,734.00 Da), and the yield was established to be ∼10 mg/$L_{cell\ culture}$. Enzymatic activity was calculated with kinetics direct assay and spectrophotometric readout as reported in the literature.[27,40] Human enzymes for the measurement of the compounds' off target activity were characterized as well, and *h*DHFR exhibited a k_{cat} of 1.21 ± 0.14, K_M(DHF) 5.41 ± 0.84 μM, and K_M(NADPH) 9.98 ± 1.14 μM. These data agree with previous studies.[44]

Recombinant hTS. *6xHis-h*TS (EC:2.1.1.45) was produced in *E. coli* BL21(DE3) cells and purified by exploiting the N-terminal His^6-tag, according to established protocols.[40] The synthetic gene encoding for *h*TS, optimized for *E. coli* expression, was cloned in the pQE80L expression vector within the BamHI-HindIII restriction sites (pQE80L−*h*TS plasmid). Through this plasmid vector, the target protein is produced as His^6-tag protein allowing its purification through the IMAC technique. The pQE80L−*h*TS plasmid was used to heath-shock transform chemically competent *E. coli* BL21-(DE3) cells. Bacteria were cultured at 30 °C in LB medium (supplemented with 100 mg/L ampicillin) under vigorous aeration (220 rpm) to $OD_{600\ nm}$ value of 0.6−0.8, and then 0.1 mM IPTG was added for 4hs at 37 °C. Cells, harvested by centrifugation (3500*g*, 15 min, 8 °C), were in buffer A (25 mM HEPES pH 7.5, 30 mM NaCl) supplemented with lysozyme (0.5 mg/mL) and 0.1 mM PMSF and disrupted by sonication after 30−60 min of incubation on ice. HT-*h*TS was purified by nickel-affinity chromatography on a HisTrap FF 5 mL column (GE-Healthcare), performing the elution from the matrix using buffer A supplemented with 250−500 mM imidazole. Collected fractions including the target protein, identified by SDS-PAGE analysis, were combined and subjected to Hi trap size exclusion to remove imidazole. The high purity of the final sample of HT-*h*TS was confirmed by SDS-PAGE analysis as >98% and high-resolution MS (aa 325, M.W. 37,114 Da, per monomer), and the yield was established to ∼20 mg/$L_{cell\ culture}$. Human enzymes for the measurement of the compounds' off target activity were characterized as well, and hTS k_{cat} is 0.98 ± 0.03 s^{-1}, K_M(dUMP) 13.44 ± 1.21 μM, and K_M(THF) 5.87 ± 0.98 μM. These data agree with the literature.[45]

Protein Crystallization. *Tb*PTR1 was crystallized at room temperature by the sitting-drop vapor diffusion technique, as described elsewhere.[46] Briefly, well-ordered *Tb*PTR1 crystals grew within a few days (to final dimensions of ∼600 μm × 400

https://doi.org/10.1021/acsinfecdis.4c00113
ACS Infect. Dis. 2024, 10, 2755−2774

μm × 100 μm) in drops prepared by mixing equal volumes of protein (20−40 mg/mL, in 20 mM TRIS, pH 7.5 and 10 mM DTT) and precipitant (1.6−2.5 M sodium acetate and 0.1 M sodium citrate, pH 5) solutions. *Tb*PTR1−NADP(H)−inhibitor complexes were obtained by the soaking technique; compound solutions (in DMSO) were added to a final concentration of 4−5 mM directly to the drops containing preformed protein crystals. After 1−2 h exposure, crystals were washed in the cryoprotectant solution (30% v/v glycerol, 2 M sodium acetate, and 0.1 M sodium citrate, pH 5) and flash frozen in liquid nitrogen.

The purified sample of *Tb*DHFR (6 mg/mL, in buffer A) was cocrystallized with the cofactor NADPH (2 mM) and the inhibitor **1g** (4 mM), using the microbatch method at room temperature. Crystallization drops were prepared by mixing equal volumes (1.5 μL) of the ternary complex solution and the precipitant, 35% (w/v) PEG4000, 50 mM ammonium sulfate, 50 mM bis−tris, pH 6.5, under Al's oil. Needle-shaped crystals, grown within a few days, were transferred to the cryoprotect (precipitant supplemented with 25% v/v PEG400) and then flash frozen in liquid nitrogen. The cocrystallization of *Tb*DHFR (6 mg/mL, in buffer A) in complex with the cofactor NADPH (2 mM) and the inhibitor **2g** (2−4 mM) was also attempted using both the microbatch method and the vapor diffusion technique, at room temperature. Crystallization trials were performed in both methods using precipitant solutions including different concentrations of PEGs (10−40% (w/v) of either PEG3350, PEG4600, or PEG8000) and ammonium sulfate (10−200 mM), in 50 mM bis-tris, pH 6.0−7.0. Small needle-shaped crystals were obtained using the microbatch under the oil (Al's oil) technique, which showed only poor diffraction when tested using synchrotron radiation.

X-ray Crystallography. Diffraction data were collected using synchrotron radiation at Diamond Light Source (DLS, Didcot, United Kingdom) beamlines I04 and I24, equipped with the Dectris Eiger2 XE 16 M detector and a Pilatus3 6 M detector, respectively, and at European Synchrotron Radiation Facility (ESRF, France) beamline ID23-1, equipped with Eiger X 9M. X-ray diffraction data were integrated using XDS[47] and scaled with Aimless[48,49] from the CCP4 suite.[50] *Tb*PTR1 crystals belong to the monoclinic space group $P2_1$, with only slight variations in the cell parameters among crystals. Four enzyme chains, forming a functional *Tb*PTR1 tetramer, populate the crystal asymmetric unit (ASU). *Tb*DHFR crystals belong to the orthorhombic space group $P2_12_12_1$ with one protein monomer in the crystal ASU. Data collection and processing statistics are reported in Table S1. The structures were solved by molecular replacement using the software Molrep.[51] For *Tb*PTR1 structures, a whole enzyme tetramer (PDB id 6TBX[21]) was used as the search model; on the other hand, a single monomer (PDB id 3QFX[26]) was adopted as the model for *Tb*DHFR. All structures were refined with the program REFMAC5[52] from the CCP4 suite. The molecular graphic software Coot[53] was used for electron density inspection and model manipulation. Since early cycles of refinement, large positive maxima were observed in both cofactor and substrate sites, having shapes and sizes coherent with their population by NADP(H) and inhibitor molecules. Exogenous ligands were modeled in these sites according to the visible electron densities, and their occupancies were adjusted and refined to values resulting in atomic-displacement parameters close to those of the neighboring protein atoms in fully occupied sites. The automatic placement of water molecules was performed in all structures with the ARPwARP suite.[54] The final models were inspected manually and checked with the programs Coot and Procheck;[55] refinement and validation statistics are summarized in Table S2. Coordinates and structure factors were validated and deposited in the PDB, under accession codes 8RHT (*Tb*DHFR−NADP(H)−**1g** (P25)), 8RHU (*Tb*PTR1−NADP(H)−**1g** (P25)), 8RHV (*Tb*PTR1−NADP(H)−**1f** (P30)), 8RHW (*Tb*PTR1−NADP-(H)−**2f** (P31)), 8RHX (*Tb*PTR1−NADP(H)−**2d** (P32)), and 8RHY (*Tb*PTR1−NADP(H)−**2c** (P34)). Figures were generated with CCP4 mg.[56]

Enzyme Inhibition Assays. Compounds to be tested were dissolved in DMSO at 100 μM stock solution and 1:10 dilutions. DMSO final concentration in the sample was <4% vol/vol in order to not interfere with the reaction rate during inhibition assays.

***Tb*PTR1 Inhibition Assay.** A direct kinetic assay was performed to monitor NADPH consumption over time with a Jasco V730 double-beam spectrophotometer. Thawed protein was incubated in 40 mM citrate buffer pH 3.7 at a final concentration of 30 nM and with the endogenous substrate dihydrobiopterin at a final concentration of 27 μM, in a Kartell semimicro disposable polystyrene plastic cuvette (Kartell LABWARE, Milan, Italy). The inhibitor was added at increasing final concentration from the DMSO initial stocks and incubated with the enzyme for 15 min at room temperature. Every compound was assayed in duplicate and in parallel with the noninhibited protein control assay. NADP(H) solution at a final concentration of 134 μM was then added to the cuvette to start the reaction, and the Δ(OD)/min at 340 nm was recorded over 180s at 25 °C and DHB of 27 μM.[27] Six different concentrations were measured and plotted with a 3PL fitting. A 95% interval of confidence (CI) of fitting was employed to calculate the associated standard error per each curve fitting, and a t-student was run per each duplicate with a p-value $\leq$ 0.05. GraphPad Prism Suite (2021) was employed for data fitting and statistics. Associated K_i for each inhibitor was calculated from IC_{50} assuming a competitive, nontight binding inhibition mode, according to the kinetic assumption that $IC_{50} = K_i(1 + [S]/[K_m])$.[57] Pyrimethamine ($K_i$ = 0.016 μM), cycloguanil (K_i = 4.16 μM), and methotrexate (K_i = 0.138 μM) were used as reference inhibitors.

***Tb*DHFR-TS Inhibition Assay versus the DHFR Domain.** A direct kinetic assay was performed to monitor NADPH consumption over time with a Jasco V730 double-beam spectrophotometer. Thawed protein was incubated in TES buffer (100 mM TES, 50 mM $MgCl_2$, 13 mM CH_2O, 2 mM EDTA, 150 mM 2-mercaptoethanol, pH 7.4) at a final concentration of 30 nM and with the endogenous substrate dihydrofolic acid at a final concentration of 30 μM, in a Kartell semimicro disposable polystyrene plastic cuvette (Kartell LABWARE, Milan, Italy). The inhibitor was added at increasing final concentration from the DMSO initial stocks and incubated with the enzyme for 15 min at room temperature. Every compound was assayed in duplicate and in parallel with the noninhibited protein control assay. NADP(H) solution at a final concentration of 200 μM was then added to the cuvette to start the reaction, and the Δ(OD)/min at 340 nm was recorded over 180 s at 25 °C.[27] Six different concentrations were measured and plotted with a 3PL fitting (3 parameters logistic regression). A 95% interval of confidence (CI) of fitting was employed to calculate the

https://doi.org/10.1021/acsinfecdis.4c00113
ACS Infect. Dis. 2024, 10, 2755−2774

associated standard error per each curve fitting, and a *t*-student was run per each duplicate with a *p*-value ≤0.05. GraphPad Prism Suite (2021) was employed for data fitting and statistics. Associated K_i for each inhibitor was calculated from IC_{50} assuming a competitive, nontight binding inhibition mode, according to the kinetic assumption that $IC_{50} = K_i (1 + [S]/[K_m])$.[57] Pyrimethamine ($K_i$ = 0.038 μM), cycloguanil (K_i = 0.256 μM), and methotrexate (K_i = 0.006 μM) were used as reference inhibitors.

***Tb*DHFR-TS Inhibition Assay versus the TS Domain.** A direct kinetic assay was performed to monitor the conversion of *N*5,*N*10-methylene tetrahydrofolate to dihydrofolate over time with a Jasco V730 double-beam spectrophotometer. Thawed protein was incubated in TES buffer (100 mM TES, 50 mM $MgCl_2$, 13 mM CH_2O, 2 mM EDTA, 150 mM, 2-mercaptoethanol, pH 7.4) at a final concentration of 30 nM and with the endogenous substrate *N*5,*N*10-methylenetetrahydrofolate (mTHF) at a final concentration of 25 μM, in a Kartell semimicro disposable polystyrene plastic cuvette (Kartell LABWARE, Milan, Italy). The inhibitor was added at increasing final concentration from the DMSO initial stocks, and the mixture was incubated with the protein for 15 min at room temperature. Every compound was assayed in duplicate and in parallel with the noninhibited protein control assay. Deoxyuridine-monophosphate solution (dUMP) at a final concentration of 80 μM (20xK_M—saturation concentration) was then added to the cuvette to start the reaction, and the Δ(OD)/min at 340 nm was recorded over 180 s at 25 °C.[40] Six different concentrations per curve were measured and plotted with a 3PL fitting (three-parameter logistic regression model). A 95% interval of confidence (CI) of fitting was employed to calculate the associated standard error per each curve fitting, and a *t*-student was run per each duplicate with a *p*-value ≤0.05. GraphPad Prism Suite (2021) was employed for data fitting and statistics. Associated K_i for each inhibitor was calculated from IC_{50} assuming a full competitive, nontight binding inhibition mode, according to the kinetic assumption that $IC_{50} = K_i (1 + [S]/[K_m])$.[57] Methotrexate ($K_i$ = 46.3 μM) was used as the reference inhibitor.

***h*DHFR Inhibition Assay.** A direct kinetic assay was performed to monitor the conversion of *N*5,*N*10-methylene tetrahydrofolate to dihydrofolate over time with a Jasco V730 double-beam spectrophotometer. Thawed protein was incubated in TES buffer (100 mM TES, 50 mM $MgCl_2$, 13 mM CH_2O, 2 mM EDTA, 150 mM 2-mercaptoethanol, pH 7.4) at a final concentration of 100 nM and with the endogenous substrate dihydrofolic acid at a final concentration of 50 μM, in a Kartell semimicro disposable polystyrene plastic cuvette (Kartell LABWARE, Milan, Italy). The inhibitor was added at increasing final concentration from the DMSO initial stocks, and the mixture was incubated with the protein for 15 min at room temperature. Every compound was assayed in duplicate and in parallel with the noninhibited protein control assay. NADP(H) solution at a final concentration of 200 μM was then added to the cuvette to start the reaction, and the Δ(OD)/min at 340 nm was recorded over 180 s at 25 °C.[27] Six different concentrations per curve were measured and plotted with a 3PL fitting (three-parameter logistic regression model). A 95% interval of confidence (CI) of fitting was employed to calculate the associated standard error per each curve fitting, and a *t*-student was run per each duplicate with a *p*-value ≤0.05. GraphPad Prism Suite (Prism 9.01, 2021) was employed for data fitting and statistics. Associated K_i for each inhibitor was calculated from IC_{50} assuming a full competitive, nontight binding inhibition mode, according to the kinetic assumption that $IC_{50} = K_i \times (1 + [S]/[K_m])$.[57] Pyrimethamine ($K_i$ = 0.247 μM), cycloguanil (K_i = 0.396 μM), and methotrexate (K_i = 0.004 μM) were used as reference inhibitors.

***h*TS Inhibition Assay.** A direct kinetic assay was performed to monitor the conversion of *N*5,*N*10-methylene tetrahydrofolate to dihydrofolate over time with a Jasco V730 double-beam spectrophotometer. Thawed protein was incubated in TES buffer (100 mM TES, 50 mM $MgCl_2$, 13 mM CH_2O, 2 mM EDTA, 150 mM, 2-mercaptoethanol, pH 7.4) at a final concentration of 30 nM and with the endogenous substrate *N*5,*N*10-methylenetetrahydrofolate (mTHF) at a final concentration of 25 μM, in a Kartell semimicro disposable polystyrene plastic cuvette (Kartell LABWARE, Milan, Italy). The inhibitor was added at increasing final concentration from the DMSO initial stocks, and the mixture was incubated with the protein for 15 min at room temperature. Every compound was assayed in duplicate and in parallel with the noninhibited protein control assay. Deoxyuridine-monophosphate solution (dUMP) at a final concentration of 80 μM (saturation concentration) was then added to the cuvette to start the reaction, and the Δ(OD)/min at 340 nm was recorded over 180 s at 25 °C.[40] Six different concentrations per curve were measured and plotted with a 3PL fitting (three-parameter logistic regression model). A 95% interval of confidence (CI) of fitting was employed to calculate the associated standard error per each curve fitting, and a *t*-student was run per each duplicate with a *p*-value ≤0.05. GraphPad Prism Suite (2021) was employed for data fitting and statistics. Associated K_i for each inhibitor was calculated from IC_{50} assuming a full competitive, nontight binding inhibition mode, according to the kinetic assumption that $IC_{50} = K_i \times (1 + [S]/[K_m])$.[57] Pyrimethamine ($K_i$ = 11.8 μM), cycloguanil (K_i = 22.5 μM), and methotrexate (K_i = 1.57 μM) were used as reference inhibitors.

***Lm*DHFR Inhibition Assay.** A direct kinetic assay was performed to monitor NADPH consumption over time with a Jasco V730 double-beam spectrophotometer. Thawed protein was incubated in TES buffer (100 mM TES, 50 mM $MgCl_2$, 13 mM CH_2O, 2 mM EDTA, 150 mM 2-mercaptoethanol, pH 7.4) at a final concentration of 30 nM and with the endogenous substrate dihydrofolic acid at a final concentration of 60 μM, in a Kartell semimicro disposable polystyrene plastic cuvette (Kartell LABWARE, Milan, Italy). The inhibitor was added at increasing final concentration from the DMSO initial stocks, and the mixture was incubated with the protein for 15 min at room temperature. Every compound was assayed in duplicate and in parallel with the noninhibited protein control assay. NADP(H) solution at a final concentration of 100 μM was then added to the cuvette to start the reaction, and the Δ(OD)/min at 340 nm was recorded over 180 s at 25 °C.[40] Six different concentrations per curve were measured and plotted with a 3PL fitting (three-parameter logistic regression model). A 95% interval of confidence (CI) of fitting was employed to calculate the associated standard error per each curve fitting, and a *t*-student was run per each duplicate with a *p*-value ≤0.05. GraphPad Prism Suite (2021) was employed for data fitting and statistics. Associated K_i for each inhibitor was calculated from IC_{50} assuming a full competitive, nontight binding inhibition mode, according to the kinetic assumption that $IC_{50} = K_i \times (1 + [S]/[K_m])$.[57]

https://doi.org/10.1021/acsinfecdis.4c00113
ACS Infect. Dis. 2024, 10, 2755−2774

***Tc*DHFR Inhibition Assay.** A direct kinetic assay was performed to monitor NADPH consumption over time with a Jasco V730 double-beam spectrophotometer. Thawed protein was incubated in TES buffer (100 mM TES, 50 mM $MgCl_2$, 13 mM CH_2O, 2 mM EDTA, 150 mM 2-mercaptoethanol, pH 7.4) at a final concentration of 28 nM and with the endogenous substrate dihydrofolic acid at a final concentration of 60 μM, in a Kartell semimicro disposable polystyrene plastic cuvette (Kartell LABWARE, Milan, Italy). The inhibitor was added at increasing final concentration from the DMSO initial stocks, and the mixture was incubated with the protein for 15 min at room temperature. Every compound was assayed in duplicate and in parallel with the noninhibited protein control assay. NADP(H) solution at a final concentration of 100 μM was then added to the cuvette to start the reaction, and the Δ(OD)/min at 340 nm was recorded over 180 s at 25 °C.[40] Six different concentrations per curve were measured and plotted with a 3PL fitting (three-parameter logistic regression model). A 95% interval of confidence (CI) of fitting was employed to calculate the associated standard error per each curve fitting, and a t-student was run per each duplicate with a p-value $\leq$0.05. GraphPad Prism Suite (2021) was employed for data fitting and statistics. Associated K_i for each inhibitor was calculated from IC_{50} assuming a full competitive, nontight binding inhibition mode, according to the kinetic assumption that $IC_{50} = K_i \times (1 + [S]/[K_m])$.[57]

Inhibition Pattern Determination. The inhibition pattern was determined for **2g** according to the Dixon's plot procedure. The inhibitor was assayed at 0.33, 0.67, 1.67, 2.00, 6.67, and 13.33 μM against *Tb*DHFR-TS in the presence of five increasing concentrations of DHB (8.6, 16.0, 22.8, 26.7, and 30 μM). The reciprocal of the v_0 was plotted against the concentration of the inhibitor in a Dixon's plot and the intersection point of each linear fitting was graphically calculated, which represents a K_i value of 0.043 μM[58−60] (Figure S1). The model demonstrates the competitive nature of these derivatives for the orthosteric site of the reductase domain of *Tb*DHFR-TS. Raw data used to extrapolate the model are reported in the Supporting Information, Tables S5−S7.

Parasite and Cell Cultures. The reference strain *L. infantum* MHOM/TN/80/IPT1 (WHO international reference strain) was purchased from ATCC (ATCC 50134) and cultured in Evans's Modified Tobie Medium (EMTM) at 26−28 °C. During the treatment with the amino dihydrotriazine motif of cycloguanil derivative compounds, the parasites were maintained in the RPMI-PY medium as previously described.[61]

T. brucei brucei Lister 427 bloodstream forms were cultivated in the HMI-9 medium, as previously described.[62]

The human monocytic cell line THP-1 (ECACC 88081201) was cultured in the RPMI-1640 medium supplemented with 10% heat-inactivated fetal bovine serum (FBS), 2 mM L-glutamine, 10 g/L nonessential amino acid, 1 mM sodium pyruvate, 100 μg/mL streptomycin, and 100 U/L penicillin. Cells were maintained in a humidified incubator at 37 °C with 5% CO_2. All cell culture reagents were purchased from Sigma-Aldrich (St. Louis, MO, USA).

In Vitro Evaluation of Activity toward the *T. brucei* Parasite. The efficacy of compounds against the *T. brucei* bloodstream forms was evaluated by a modified resazurin assay.[40] *T. brucei* bloodstream forms were added to an equal volume of serial dilutions of the compound in the HMI-9 medium until a cell density of 5×10^3/mL was achieved. The plates were included as positive controls for antiparasitic activity 10 nM pentamidine and as negative control parasites without drugs. All of the assays included a dose response curve for pentamidine. After incubation for 72 h at 37 °C and 5% CO_2, 20 μL of a 0.5 mM resazurin solution was added, and the plates were incubated for an additional 4 h under the same conditions. Fluorescence was measured at 540 and 620 nm (excitation and emission wavelengths, respectively) using a Synergy 2 Multi-Mode Reader (Biotek, USA). The antitrypanosome activity was calculated as % Antiparasitic activity = 1 − [(Test Value − Mean Neg)/(Mean Pos − Mean Neg) × 100]. The antitrypanosome effect was assessed by determining the EC_{50} value (concentration required to inhibit parasite growth by 50%) and calculated by nonlinear regression analysis using GraphPad Prism version 9 for Windows (GraphPad Software, USA). The reported EC_{50} values correspond to the average of the results obtained in at least three independent experiments.

***L. infantum* Promastigotes Viability Assay.** The compound activity was first evaluated on late log/stationary phase *L. infantum* promastigotes resuspended in 96-well plates (100 μL/well) in a complete RPMI-PY medium with a density of 2.5×10^6 parasites/mL. The antiparasitic activity was initially investigated with a single dose of 20 μM of each compound for 72 h at 26 °C. To analyze the dose−response, all compounds that showed an antiparasitic activity >50% at 20 μM were further tested at scalar dilutions 1:2 or 2:3 (from 20 to 0.31 μM) on promastigotes. As the positive control, the antileishmanial drug MLF (Sigma-Aldrich, Milan, Italy) was included. Each condition was carried out in duplicate. The promastigotes viability was evaluated using the CellTiter 96H aqueous nonradioactive cell proliferation assay (Promega, Madison, Wisconsin, USA), as previously reported.[61] The efficacy of selected compounds was evaluated by determining the IC_{50} values using the nonlinear regression curves in GraphPad Prism 8.0 (GraphPad Software, Inc., San Diego, CA, USA). The equation used for data fitting was $Y = 100/(1 + 10^{((\text{Log IC50-X})\times\text{HillSlope})})$ (hillslope not constrained), where X = log of concentration and Y = normalized response.

Cytotoxicity Assay. The effect of compounds on THP-1-derived macrophages was assessed by a modified colorimetric MTT assay (3-(4,5-dimethylthiazol-2-yl)-2,5-diphenyl tetrazolium bromide).[40] Briefly, 5×10^5 THP-1 cells were differentiated into macrophages by addition of 20 ng/mL of phorbol-myristate 13-acetate (PMA, Sigma-Aldrich) for 48h, followed by replacement with a fresh medium for 24 h. Cells were incubated with compounds ranging from 100 to 12.5 μM after dilution in RPMI complete medium containing a maximum amount of 1% DMSO. As positive controls, cells without compounds were used, and as blank, wells with media only, without cells, were used. After incubation for 72 h at 37 °C, 5% CO_2, the medium was removed and a 0.5 mg/mL MTT solution was added. Plates were incubated for an additional 4 h to allow viable cells to convert MTT into a purple formazan product. Solubilization of formazan crystals was achieved by addition of 2-propanol, and absorbance was read at 570 nm using a Synergy 2 multimode reader (Biotek). Viability was calculated as % viability = [(Test Value − blank)/(Mean Pos − blank) × 100]. Cytotoxicity was evaluated by determination of CC_{50} values (drug concentration that reduced the percentage of viable cells to 50%).

Statistical Analysis. The statistical analysis for the in vivo experiments was performed by Ordinary one-way ANOVA

https://doi.org/10.1021/acsinfecdis.4c00113
ACS Infect. Dis. 2024, 10, 2755−2774

with Dunnett's multiple comparisons test (single pooled variance). For in vitro studies, the evaluation of IC_{50} in promastigotes and CC_{50} in mammalian cells following compound treatment was performed by nonlinear regression analysis and expressed as means and 95% confidence interval. Cytotoxicity statistical analysis on infected cells was performed using two-way ANOVA followed by Dunnett's multiple comparisons test. All statistical tests were performed using GraphPad Prism version 8.0.1 (GraphPad Software, Inc., La Jolla, CA, USA). A p-value of ≤ 0.05 was considered significant.

■ ASSOCIATED CONTENT

Supporting Information

The Supporting Information is available free of charge at https://pubs.acs.org/doi/10.1021/acsinfecdis.4c00113.

*Tb*DHFR and *Tb*PTR1: data collection and processing (Table S1); structure-solution, and refinement statistics (Table S2); inhibitor and cofactor occupancies within the catalytic cavity (Table S3). Description of the overall structure of *Tb*PTR1 (apoenzyme). In silico estimation of lipophilicity (Log $P_{o/w}$) of the investigated compounds and known antifolate drugs by Swiss ADME (Table S4). Inhibition pattern determination for **2g** according to the Dixon's plot procedure (Figure S1 and Tables S5−S7). ^{1}H and ^{13}C NMR spectra of the investigated compounds. Representative ^{1}H and NOESY spectra, and HPLC chromatogram of compound **1f**, such as the mixture of isomers **1f-I and 1f-II** (PDF)

■ AUTHOR INFORMATION

Corresponding Author

Michele Tonelli − *Department of Pharmacy, University of Genoa, Genoa 16132, Italy;* orcid.org/0000-0003-1518-2890; Email: michele.tonelli@unige.it

Authors

Valeria Francesconi − *Department of Pharmacy, University of Genoa, Genoa 16132, Italy*

Marco Rizzo − *Department of Pharmacy, University of Genoa, Genoa 16132, Italy*

Cecilia Pozzi − *Department of Biotechnology, Chemistry and Pharmacy, University of Siena, Siena 53100, Italy; Consorzio Interuniversitario Risonanze Magnetiche di Metallo Proteine (CIMMP), Sesto Fiorentino (FI) 50019, Italy;* orcid.org/0000-0003-2574-3911

Lorenzo Tagliazucchi − *Department of Life Science, University of Modena and Reggio Emilia, Modena 41125, Italy; Doctorate School in Clinical and Experimental Medicine (CEM), University of Modena and Reggio Emilia, Modena 41125, Italy;* orcid.org/0000-0002-7244-7106

Claude U. Konchie Simo − *Department of Life Science, University of Modena and Reggio Emilia, Modena 41125, Italy*

Giulia Saporito − *Department of Life Science, University of Modena and Reggio Emilia, Modena 41125, Italy*

Giacomo Landi − *Department of Biotechnology, Chemistry and Pharmacy, University of Siena, Siena 53100, Italy*

Stefano Mangani − *Department of Biotechnology, Chemistry and Pharmacy, University of Siena, Siena 53100, Italy;* orcid.org/0000-0003-4824-7478

Anna Carbone − *Department of Pharmacy, University of Genoa, Genoa 16132, Italy;* orcid.org/0000-0002-6767-2376

Silvia Schenone − *Department of Pharmacy, University of Genoa, Genoa 16132, Italy*

Nuno Santarém − *i3S - Institute for Research and Innovation in Health, University of Porto, Porto 4200-135, Portugal*

Joana Tavares − *i3S - Institute for Research and Innovation in Health, University of Porto, Porto 4200-135, Portugal*

Anabela Cordeiro-da-Silva − *i3S - Institute for Research and Innovation in Health, University of Porto, Porto 4200-135, Portugal; Department of Life Science, Faculty of Pharmacy, University of Porto, Porto 4050-313, Portugal;* orcid.org/0000-0003-2392-6087

Maria Paola Costi − *Department of Life Science, University of Modena and Reggio Emilia, Modena 41125, Italy;* orcid.org/0000-0002-0443-5402

Complete contact information is available at: https://pubs.acs.org/10.1021/acsinfecdis.4c00113

Author Contributions

V.F. and M.R.: these authors contributed equally. The manuscript was written through contributions of all authors. All authors have given approval to the final version of the manuscript.

Funding

N.S. is an assistant researcher funded by national funds through FCT and cofunded through the European Social Fund within the Human Potential Operating Programme 2021.04285.CEECIND.

Notes

The authors declare no competing financial interest.

■ ACKNOWLEDGMENTS

M. Tonelli acknowledges the dedicated technical assistance of Dr. Anna Salis (Department of Experimental Medicine, University of Genoa) with the HPLC analysis. This article is based upon work from COST Action One Health drugs against parasitic vector-borne diseases in Europe and beyond (OneHealthdrugs) CA21111, supported by COST (European Cooperation in Science and Technology).

■ ABBREVIATIONS

ACN, acetonitrile; CC_{50}, 50% cytotoxic concentration; CytC, cytochrome *C*; COSY, correlation spectroscopy; Cyc, cycloguanil; DHF, dihydrofolate; DHFR, dihydrofolate reductase; DHFR-TS, dihydrofolate reductase-thymidylate synthase; DMSO, dimethyl sulfoxide; dTMP, deoxythymidine monophosphate; dUMP, deoxyuridine monophosphate; EC_{50}, 50% effective concentration; EMTM, Evans's modified Tobie medium; HAT, Humana African trypanosomiasis; H2B, dihydrobiopterin; H4B, tetrahydrobiopterin; hDHFR, human dihydrofolate reductase; HMI-9 medium, Hirumi's modified Iscove's medium; hTS, human thymidylate synthase; IMAC, immobilized metal affinity chromatography; *L. infantum*, *Leishmania infantum*; *L. major*, *Leishmania major*; MLF, miltefosine; mTHF, methylene tetrahydrofolate; MTT assay, 3-[4,5-dimethylthiazol-2-yl]-2,5-diphenyl tetrazolium bromide assay; MTX, methotrexate; NADP(H), nicotinamide adenine dinucleotide phosphate and its reduced form; NOESY, nuclear Overhauser effect spectroscopy; NTDs, neglected tropical diseases; PDB, protein data bank; PENT, pentamidine; PMSF,

https://doi.org/10.1021/acsinfecdis.4c00113
ACS Infect. Dis. 2024, 10, 2755−2774

mM phenylmethylsulfonyl fluoride; PTR1, pteridine reductase type 1; Pyr, pyrimethamine; qH2B, quinonoid dihydrobiopterin; *T. cruzi*, *Trypanosoma cruzi*; TbTS, *Trypanosoma brucei* thymidylate synthase; TES buffer, 2-{[1,3-dihydroxy-2-(hydroxymethyl)propan-2-yl]amino}ethane-1-sulfonic acid buffer; THP-1, human monocytic cell line

REFERENCES

(1) *Neglected tropical diseases -- GLOBAL*. https://www.who.int/health-topics/neglected-tropical-diseases (accessed May 2023).

(2) Pereira, M. A.; Santos-Gomes, G. Parasitic Infection and Immunity-A Special Biomedicines Issue. *Biomedicines* **2022**, *10* (10), 2547.

(3) Büscher, P.; Cecchi, G.; Jamonneau, V.; Priotto, G. Human African Trypanosomiasis. *Lancet* **2017**, *390* (10110), 2397−2409.

(4) *Trypanosomiasis, human African (sleeping sickness)*. https://www.who.int/news-room/fact-sheets/detail/trypanosomiasis-human-african-(sleeping-sickness) (accessed May 2023).

(5) Álvarez-Rodríguez, A.; Jin, B.-K.; Radwanska, M.; Magez, S. Recent Progress in Diagnosis and Treatment of Human African Trypanosomiasis Has Made the Elimination of This Disease a Realistic Target by 2030. *Front. Med.* **2022**, *9*, No. 1037094, DOI: 10.3389/fmed.2022.1037094.

(6) Baker, C. H.; Welburn, S. C. The Long Wait for a New Drug for Human African Trypanosomiasis. *Trends Parasitol.* **2018**, *34* (10), 818−827.

(7) De Koning, H. P. The Drugs of Sleeping Sickness: Their Mechanisms of Action and Resistance, and a Brief History. *Trop. Med. Infect. Dis.* **2020**, *5* (1), 14.

(8) Kasozi, K. I.; MacLeod, E. T.; Ntulume, I.; Welburn, S. C. An Update on African Trypanocide Pharmaceutics and Resistance. *Front. Vet. Sci.* **2022**, *9*, No. 828111.

(9) Lee, S.-M.; Kim, M.-S.; Hayat, F.; Shin, D. Recent Advances in the Discovery of Novel Antiprotozoal Agents. *Molecules* **2019**, *24* (21), 3886.

(10) Brindha, J.; Balamurali, M. M.; Chanda, K. An Overview on the Therapeutics of Neglected Infectious Diseases-Leishmaniasis and Chagas Diseases. *Front. Chem.* **2021**, *9*, No. 622286.

(11) Souto, E. B.; Dias-Ferreira, J.; Craveiro, S. A.; Severino, P.; Sanchez-Lopez, E.; Garcia, M. L.; Silva, A. M.; Souto, S. B.; Mahant, S. Therapeutic Interventions for Countering Leishmaniasis and Chagas's Disease: From Traditional Sources to Nanotechnological Systems. *Pathogens* **2019**, *8* (3), 119.

(12) Sehrawat, R.; Rathee, P.; Khatkar, S.; Akkol, E.; Khayatkashani, M.; Nabavi, S. M.; Khatkar, A. Dihydrofolate Reductase (DHFR) Inhibitors: A Comprehensive Review. *Curr. Med. Chem.* **2024**, *31* (7), 799−824.

(13) Pöhner, I.; Quotadamo, A.; Panecka-Hofman, J.; Luciani, R.; Santucci, M.; Linciano, P.; Landi, G.; Di Pisa, F.; Dello Iacono, L.; Pozzi, C.; Mangani, S.; Gul, S.; Witt, G.; Ellinger, B.; Kuzikov, M.; Santarem, N.; Cordeiro-da-Silva, A.; Costi, M. P.; Venturelli, A.; Wade, R. C. Multitarget, Selective Compound Design Yields Potent Inhibitors of a Kinetoplastid Pteridine Reductase 1. *J. Med. Chem.* **2022**, *65* (13), 9011−9033.

(14) Shamshad, H.; Bakri, R.; Mirza, A. Z. Dihydrofolate Reductase, Thymidylate Synthase, and Serine Hydroxy Methyltransferase: Successful Targets against Some Infectious Diseases. *Mol. Biol. Rep.* **2022**, *49* (7), 6659−6691.

(15) Vickers, T. J.; Beverley, S. M. Folate Metabolic Pathways in Leishmania. *Essays Biochem.* **2011**, *51*, 63−80.

(16) Bigot, S.; Leprohon, P.; Ouellette, M. Delving in Folate Metabolism in the Parasite Leishmania Major through a Chemogenomic Screen and Methotrexate Selection. *PLoS Negl. Trop. Dis.* **2023**, *17* (6), No. e0011458.

(17) Gibson, M. W.; Dewar, S.; Ong, H. B.; Sienkiewicz, N.; Fairlamb, A. H. Trypanosoma Brucei DHFR-TS Revisited: Characterisation of a Bifunctional and Highly Unstable Recombinant Dihydrofolate Reductase-Thymidylate Synthase. *PLoS Negl. Trop. Dis.* **2016**, *10* (5), No. e0004714.

(18) Cullia, G.; Tamborini, L.; Conti, P.; De Micheli, C.; Pinto, A. Folates in Trypanosoma Brucei: Achievements and Opportunities. *ChemMedChem.* **2018**, *13* (20), 2150−2158.

(19) Panecka-Hofman, J.; Poehner, I.; Wade, R. C. Anti-Trypanosomatid Structure-Based Drug Design − Lessons Learned from Targeting the Folate Pathway. *Expert Opin. Drug Discovery* **2022**, *17* (9), 1029−1045.

(20) Bhattacharya, A.; Leprohon, P.; Ouellette, M. Combined Gene Deletion of Dihydrofolate Reductase-Thymidylate Synthase and Pteridine Reductase in Leishmania Infantum. *PLoS Negl. Trop. Dis.* **2021**, *15* (4), No. e0009377.

(21) Landi, G.; Linciano, P.; Tassone, G.; Costi, M. P.; Mangani, S.; Pozzi, C. High-Resolution Crystal Structure of Trypanosoma Brucei Pteridine Reductase 1 in Complex with an Innovative Tricyclic-Based Inhibitor. *Acta Crystallogr., D: Struct. Biol.* **2020**, *76* (Pt 6), 558−564.

(22) Dize, D.; Tata, R. B.; Keumoe, R.; Kouipou Toghueo, R. M.; Tchatat, M. B.; Njanpa, C. N.; Tchuenguia, V. C.; Yamthe, L. T.; Fokou, P. V. T.; Laleu, B.; Duffy, J.; Bishop, O. T.; Boyom, F. F. Preliminary Structure-Activity Relationship Study of the MMV Pathogen Box Compound MMV675968 (2,4-Diaminoquinazoline) Unveils Novel Inhibitors of Trypanosoma Brucei Brucei. *Molecules* **2022**, *27* (19), 6574.

(23) Linciano, P.; Quotadamo, A.; Luciani, R.; Santucci, M.; Zorn, K. M.; Foil, D. H.; Lane, T. R.; Cordeiro da Silva, A.; Santarem, N.; Moraes, C. B.; Freitas-Junior, L.; Wittig, U.; Mueller, W.; Tonelli, M.; Ferrari, S.; Venturelli, A.; Gul, S.; Kuzikov, M.; Ellinger, B.; Reinshagen, J.; Ekins, S.; Costi, M. P. High-Throughput Phenotypic Screening and Machine Learning Methods Enabled the Selection of Broad-Spectrum Low-Toxicity Antitrypanosomatidic Agents. *J. Med. Chem.* **2023**, *66* (22), 15230−15255.

(24) Linciano, P.; Pozzi, C.; Tassone, G.; Landi, G.; Mangani, S.; Santucci, M.; Luciani, R.; Ferrari, S.; Santarem, N.; Tagliazucchi, L.; Cordeiro-da-Silva, A.; Tonelli, M.; Tondi, D.; Bertarini, L.; Gul, S.; Witt, G.; Moraes, C. B.; Costantino, L.; Costi, M. P. The Discovery of Aryl-2-Nitroethyl Triamino Pyrimidines as Anti-Trypanosoma Brucei Agents. *Eur. J. Med. Chem.* **2024**, *264*, No. 115946.

(25) Landi, G.; Linciano, P.; Borsari, C.; Bertolacini, C. P.; Moraes, C. B.; Cordeiro-da-Silva, A.; Gul, S.; Witt, G.; Kuzikov, M.; Costi, M. P.; Pozzi, C.; Mangani, S. Structural Insights into the Development of Cycloguanil Derivatives as Trypanosoma Brucei Pteridine-Reductase-1 Inhibitors. *ACS Infect. Dis.* **2019**, *5* (7), 1105−1114.

(26) Vanichtanankul, J.; Taweechai, S.; Yuvaniyama, J.; Vilaivan, T.; Chitnumsub, P.; Kamchonwongpaisan, S.; Yuthavong, Y. Trypanosomal Dihydrofolate Reductase Reveals Natural Antifolate Resistance. *ACS Chem. Biol.* **2011**, *6* (9), 905−911.

(27) Tassone, G.; Landi, G.; Linciano, P.; Francesconi, V.; Tonelli, M.; Tagliazucchi, L.; Costi, M. P.; Mangani, S.; Pozzi, C. Evidence of Pyrimethamine and Cycloguanil Analogues as Dual Inhibitors of Trypanosoma Brucei Pteridine Reductase and Dihydrofolate Reductase. *Pharmaceuticals* **2021**, *14* (7), 636.

(28) Mahurkar, N. D.; Gawhale, N. D.; Lokhande, M. N.; Uke, S. J.; Kodape, M. M. Benzimidazole: A Versatile Scaffold for Drug Discovery and beyond − A Comprehensive Review of Synthetic Approaches and Recent Advancements in Medicinal Chemistry. *Results Chem.* **2023**, *6*, No. 101139.

(29) Hernández-López, H.; Tejada-Rodríguez, C. J.; Leyva-Ramos, S. A Panoramic Review of Benzimidazole Derivatives and Their Potential Biological Activity. *Mini Rev. Med. Chem.* **2022**, *22* (9), 1268−1280.

(30) Tonelli, M.; Gabriele, E.; Piazza, F.; Basilico, N.; Parapini, S.; Tasso, B.; Loddo, R.; Sparatore, F.; Sparatore, A. Benzimidazole Derivatives Endowed with Potent Antileishmanial Activity. *J. Enzyme Inhib. Med. Chem.* **2018**, *33* (1), 210−226.

(31) Brishty, S. R.; Hossain, M. J.; Khandaker, M. U.; Faruque, M. R. I.; Osman, H.; Rahman, S. M. A. A Comprehensive Account on Recent Progress in Pharmacological Activities of Benzimidazole Derivatives. *Front. Pharmacol.* **2021**, *12*, No. 762807.

https://doi.org/10.1021/acsinfecdis.4c00113
ACS Infect. Dis. 2024, 10, 2755−2774

(32) Francesconi, V.; Rizzo, M.; Schenone, S.; Carbone, A.; Tonelli, M. State-of-the-Art Review on the Antiparasitic Activity of Benzimidazolebased Derivatives: Facing Malaria, Leishmaniasis, and Trypanosomiasis. *Curr. Med. Chem.* **2024**, *31* (15), 1955−1982.
(33) King, F. E.; Acheson, R. M.; Spensley, P. C. 275. Benziminazole Analogues of Paludrine. *J. Chem. Soc.* **1948**, *0*, 1366−1371.
(34) Dolzhenko, A. V.; Chui, W.-K. Synthesis of 2-Amino-s-Triazino[1,2-a]Benzimidazoles as Potential Antifolates from 2-Guanidino- and 2-Guanidino-5-Methylbenzimidazoles. *J. Heterocycl. Chem.* **2006**, *43* (1), 95−100.
(35) *SDBS-NMR-CDS-01-585*. https://sdbs.db.aist.go.jp/sdbs/cgi-bin/landingpage?spcode=NMR-CDS-01-585 (accessed October 2023).
(36) Hernández-García, R. M.; Barba-Behrens, N.; Salcedo, R.; Höjer, G. Theoretical Study of 2-Guanidinobenzimidazole. HF, MP2 and DFT Calculations. *J. Mol. Struct. THEOCHEM.* **2003**, *637* (1), 55−72.
(37) Cavazzuti, A.; Paglietti, G.; Hunter, W. N.; Gamarro, F.; Piras, S.; Loriga, M.; Allecca, S.; Corona, P.; McLuskey, K.; Tulloch, L.; Gibellini, F.; Ferrari, S.; Costi, M. P. Discovery of Potent Pteridine Reductase Inhibitors to Guide Antiparasite Drug Development. *Proc. Natl. Acad. Sci. U.S.A.* **2008**, *105* (5), 1448−1453.
(38) Nzila, A.; Ward, S. A.; Marsh, K.; Sims, P. F. G.; Hyde, J. E. Comparative Folate Metabolism in Humans and Malaria Parasites (Part I): Pointers for Malaria Treatment from Cancer Chemotherapy. *Trends Parasitol.* **2005**, *21* (6), 292−298.
(39) Daina, A.; Michielin, O.; Zoete, V. SwissADME: A Free Web Tool to Evaluate Pharmacokinetics, Drug-Likeness and Medicinal Chemistry Friendliness of Small Molecules. *Sci. Rep.* **2017**, *7*, 42717.
(40) Borsari, C.; Luciani, R.; Pozzi, C.; Poehner, I.; Henrich, S.; Trande, M.; Cordeiro-da-Silva, A.; Santarem, N.; Baptista, C.; Tait, A.; Di Pisa, F.; Dello Iacono, L.; Landi, G.; Gul, S.; Wolf, M.; Kuzikov, M.; Ellinger, B.; Reinshagen, J.; Witt, G.; Gribbon, P.; Kohler, M.; Keminer, O.; Behrens, B.; Costantino, L.; Tejera Nevado, P.; Bifeld, E.; Eick, J.; Clos, J.; Torrado, J.; Jiménez-Antón, M. D.; Corral, M. J.; Alunda, J. M.; Pellati, F.; Wade, R. C.; Ferrari, S.; Mangani, S.; Costi, M. P. Profiling of Flavonol Derivatives for the Development of Antitrypanosomatidic Drugs. *J. Med. Chem.* **2016**, *59* (16), 7598−7616.
(41) Studier, F. W. Protein Production by Auto-Induction in High Density Shaking Cultures. *Protein Expr. Purif.* **2005**, *41* (1), 207−234.
(42) Santucci, M.; Luciani, R.; Gianquinto, E.; Pozzi, C.; di Pisa, F.; Dello Iacono, L.; Landi, G.; Tagliazucchi, L.; Mangani, S.; Spyrakis, F.; Costi, M. P. Repurposing the Trypanosomatidic GSK Kinetobox for the Inhibition of Parasitic Pteridine and Dihydrofolate Reductases. *Pharmaceuticals* **2021**, *14* (12), 1246.
(43) Chitnumsub, P.; Yuvaniyama, J.; Chahomchuen, T.; Vilaivan, T.; Yuthavong, Y. Crystallization and Preliminary Crystallographic Studies of Dihydrofolate Reductase-Thymidylate Synthase from Trypanosoma Cruzi, the Chagas Disease Pathogen. *Acta Crystallogr. Sect., F: Struct. Biol. Cryst. Commun.* **2009**, *65* (Pt 11), 1175−1178.
(44) Pozzi, C.; Santucci, M.; Marverti, G.; D'Arca, D.; Tagliazucchi, L.; Ferrari, S.; Gozzi, G.; Losi, L.; Tassone, G.; Mangani, S.; Ponterini, G.; Costi, M. P. Structural Bases for the Synergistic Inhibition of Human Thymidylate Synthase and Ovarian Cancer Cell Growth by Drug Combinations. *Cancers* **2021**, *13* (9), 2061.
(45) Marverti, G.; Marraccini, C.; Martello, A.; D'Arca, D.; Pacifico, S.; Guerrini, R.; Spyrakis, F.; Gozzi, G.; Lauriola, A.; Santucci, M.; Cannazza, G.; Tagliazucchi, L.; Cazzato, A. S.; Losi, L.; Ferrari, S.; Ponterini, G.; Costi, M. P. Folic Acid-Peptide Conjugates Combine Selective Cancer Cell Internalization with Thymidylate Synthase Dimer Interface Targeting. *J. Med. Chem.* **2021**, *64* (6), 3204−3221.
(46) Di Pisa, F.; Landi, G.; Dello Iacono, L.; Pozzi, C.; Borsari, C.; Ferrari, S.; Santucci, M.; Santarem, N.; Cordeiro-da-Silva, A.; Moraes, C. B.; Alcantara, L. M.; Fontana, V.; Freitas-Junior, L. H.; Gul, S.; Kuzikov, M.; Behrens, B.; Pöhner, I.; Wade, R. C.; Costi, M. P.; Mangani, S. Chroman-4-One Derivatives Targeting Pteridine Reductase 1 and Showing Anti-Parasitic Activity. *Molecules* **2017**, *22* (3), 426.
(47) Kabsch, W. XDS. *Acta Crystallogr., D: Biol. Crystallogr.* **2010**, *66* (Pt2), 125−132.
(48) Evans, P. Scaling and Assessment of Data Quality. *Acta Crystallogr., D: Biol. Crystallogr.* **2006**, *62* (Pt 1), 72−82.
(49) Evans, P. R. An Introduction to Data Reduction: Space-Group Determination, Scaling and Intensity Statistics. *Acta Crystallogr., D: Biol. Crystallogr.* **2011**, *67* (Pt 4), 282−292.
(50) Winn, M. D.; Ballard, C. C.; Cowtan, K. D.; Dodson, E. J.; Emsley, P.; Evans, P. R.; Keegan, R. M.; Krissinel, E. B.; Leslie, A. G. W.; McCoy, A.; McNicholas, S. J.; Murshudov, G. N.; Pannu, N. S.; Potterton, E. A.; Powell, H. R.; Read, R. J.; Vagin, A.; Wilson, K. S. Overview of the CCP4 Suite and Current Developments. *Acta Crystallogr., D: Biol. Crystallogr.* **2011**, *67* (Pt 4), 235−242.
(51) Vagin, A.; Teplyakov, A. Molecular Replacement with MOLREP. *Acta Crystallogr., D: Biol. Crystallogr.* **2010**, *66* (Pt 1), 22−25.
(52) Murshudov, G. N.; Skubák, P.; Lebedev, A. A.; Pannu, N. S.; Steiner, R. A.; Nicholls, R. A.; Winn, M. D.; Long, F.; Vagin, A. A. REFMAC5 for the Refinement of Macromolecular Crystal Structures. *Acta Crystallogr., D: Biol. Crystallogr.* **2011**, *67* (Pt 4), 355−367.
(53) Emsley, P.; Lohkamp, B.; Scott, W. G.; Cowtan, K. Features and Development of Coot. *Acta Crystallogr., D: Biol. Crystallogr.* **2010**, *66* (Pt 4), 486−501.
(54) Langer, G. G.; Hazledine, S.; Wiegels, T.; Carolan, C.; Lamzin, V. S. Visual Automated Macromolecular Model Building. *Acta Crystallogr., D: Biol. Crystallogr.* **2013**, *69* (Pt 4), 635−641.
(55) Laskowski, R. A.; MacArthur, M. W.; Moss, D. S.; Thornton, J. M. PROCHECK: A Program to Check the Stereochemical Quality of Protein Structures. *J. Appl. Crystallogr.* **1993**, *26* (2), 283−291.
(56) McNicholas, S.; Potterton, E.; Wilson, K. S.; Noble, M. E. M. Presenting Your Structures: The CCP4mg Molecular-Graphics Software. *Acta Crystallogr., D: Biol. Crystallogr.* **2011**, *67* (Pt 4), 386−394.
(57) Cheng, Y.; Prusoff, W. H. Relationship between the Inhibition Constant (K1) and the Concentration of Inhibitor Which Causes 50 per Cent Inhibition (I50) of an Enzymatic Reaction. *Biochem. Pharmacol.* **1973**, *22* (23), 3099−3108.
(58) Kolhatkar, V.; Polli, J. E. Reliability of Inhibition Models to Correctly Identify Type of Inhibition. *Pharm. Res.* **2010**, *27* (11), 2433−2445.
(59) Kakkar, T.; Boxenbaum, H.; Mayersohn, M. Estimation of Ki in a Competitive Enzyme-Inhibition Model: Comparisons among Three Methods of Data Analysis. *Drug Metab. Dispos.* **1999**, *27* (6), 756−762.
(60) Walsh, R. Comparing Enzyme Activity Modifier Equations through the Development of Global Data Fitting Templates in Excel. *PeerJ.* **2018**, *6*, No. e6082.
(61) Diotallevi, A.; Scalvini, L.; Buffi, G.; Pérez-Pertejo, Y.; De Santi, M.; Verboni, M.; Favi, G.; Magnani, M.; Lodola, A.; Lucarini, S.; Galluzzi, L. Phenotype Screening of an Azole-Bisindole Chemical Library Identifies URB1483 as a New Antileishmanial Agent Devoid of Toxicity on Human Cells. *ACS Omega* **2021**, *6* (51), 35699−35710.
(62) Schlecker, T.; Schmidt, A.; Dirdjaja, N.; Voncken, F.; Clayton, C.; Krauth-Siegel, R. L. Substrate Specificity, Localization, and Essential Role of the Glutathione Peroxidase-Type Tryparedoxin Peroxidases in Trypanosoma Brucei. *J. Biol. Chem.* **2005**, *280* (15), 14385−14394.

https://doi.org/10.1021/acsinfecdis.4c00113
ACS Infect. Dis. 2024, 10, 2755−2774